ACS OMEGA

Open Access

http://pubs.acs.org/journal/acsodf

Article

Characterization of a New Hybrid Compound $(C_3H_8N_6)_2ZnCl_4{\cdot}2Cl$: X-ray Structure, Hirshfeld Surface, Vibrational, Thermal Stability, Dielectric Relaxation, and Electrical Conductivity

Sahar Zaghden, Hadhemi Ben Attia, Mohammed S. M. Abdelbaky, Abderrazek Oueslati, Santiago García-Granda, Mohamed Dammak,* and Lilia Ktari

Cite This: *ACS Omega* 2024, 9, 47597−47612

Read Online

ACCESS | Metrics & More | Article Recommendations | Supporting Information

ABSTRACT: A novel organic−inorganic material $(C_3H_8N_6)_2ZnCl_4{\cdot}2Cl$ was synthesized via a slow evaporation approach and subjected to extensive characterization. Techniques involving X-ray diffraction, SEM/EDX, Hirshfeld surface examination, IR/Raman spectroscopy, thermal behavior (TG/DTG/SDTA and DSC), and electric and dielectric studies were applied. Examination of the crystal structure reveals that the synthesized material adopts a monoclinic system, particularly belonging to the $P2_1/c$ space group with unit cell parameters a = 11.7274(3) Å, b = 6.2155(2) Å, c = 25.7877(8) Å, β = 94.27(1)°, V = 1874.50(4) Å^3, and Z = 4. Purity confirmation was established via powder X-ray diffraction analysis. Composition verification was conducted using semiquantitative EDXS analysis. The asymmetric unit comprises isolated tetrachlorozincate $[ZnCl_4]^{2-}$ anions, two $(C_3H_8N_6)^{2+}$ organic cations, and two free chlorine atoms, forming a 0D anionic network. N−H···Cl and N−H···N hydrogen bonding combined to form a 2D hydrogen-bonded network, maintaining crystal stability. Hirshfeld surface analysis elucidated intermolecular interactions, supported by 2D fingerprint plots. IR and Raman spectra analysis corroborated compound characteristics at room temperature. Thermal analysis revealed two phase transitions at 343 and 358 K, consistent with dielectric studies. Impedance spectroscopy highlighted the compound's electrical properties, confirming thermal transitions. Conductivity studies exhibited an Arrhenius behavior. Frequency-dependent dielectric constant variations and modulus studies underscored grain and grain boundary effects, confirming the effective protonic conduction in the material.

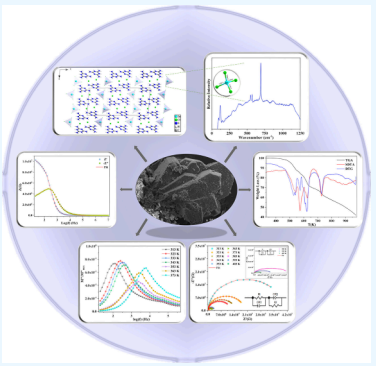

1. INTRODUCTION

Over the past decade, researchers have become increasingly fascinated by hybrid compounds that blend metal halide units with organic molecules. These compounds are attractive because they offer a unique mix of properties such as adjustable band gaps, high electrical mobility, thermal stability, magnetic or dielectric transitions, and efficient luminescence.[1−3] The organic components also provide structural variety, plastic mechanical properties, ease of processing, and potential for weak interactions. This has spurred a wealth of research, yielding many promising discoveries.[4−7] The synergy of these properties opens up diverse applications across various fields, including industry,[8] environmental science,[9,10] medicine and biology,[4,11,12] biochemistry,[13] electronics,[14−16] and chemistry.[17] These materials enable the synergy of beneficial features from both inorganic and organic molecules,[18] enabling different structural sizes such as 0D $(Me_3NOH)_2[ZnCl_4]$,[19] 1D [3-aminopiperidine]PbI_4,[20] 2D $(C_7H_{18}N_2)PbI_4$,[21] and 3D $[(CH_3)_3NCH_2F]_2[KFe(CN)_6]$.[22] They exhibit a variety of physicochemical properties, including magnetic, conductive, luminescent, catalytic, optical, nonlinear optical, biological, electrical, and ferroelectric characteristics,[23−27] which lend themselves to applications in protective coatings,[28] electrochemical science,[29] catalysis,[30] energy-related technologies,[31,32] and biomedical fields.[33]

Zinc(II)-based complexes are in high demand across fields such as chemistry, biology, pharmacology, energy transition, and materials science.[34,35] The various physical and chemical features of these materials make them highly demanded. Their characteristics encompass a broad spectrum, including magnetic and ferroelectric transitions, different levels of conductivity even reaching superconductivity, electroluminescent capabilities, and photoluminescent features. This remaining variety of features leads to their attraction in several fields.[35−40] Zinc is particularly important in organizing hybrid materials among transition metals. Zinc complexes exhibit various coordination numbers and geometries, such as tetrahedra,[41] square-bottom pyramids,[42] and octahedra,[43] due to the closed-shell nature of Zn

Received: July 19, 2024
Revised: October 25, 2024
Accepted: November 4, 2024
Published: November 20, 2024

(II) and its relatively large coordination distance. Their nontoxic nature further enhances their appeal.[40]

Melamine ($C_3H_6N_6$) is a crystalline organic compound widely used in industries such as plastics, adhesives, laminates, and flame retardants, and it is a popular material for making plates and kitchen utensils.[44−46] Recently, melamine has gained significant attention as an organic ligand for creating organic−inorganic hybrid materials.[47−52]

Our laboratory has been studying the physical characteristics and crystal structure of various organic−inorganic materials, along with recent research on metal halide compounds.[7,12,53,54] The important purpose of this investigation is to synthesize a new zinc(II) hybrid material. This compound, involving the chemical formula $(C_3H_8N_6)_2ZnCl_4{\cdot}2Cl$, employs 1,3,5-triazine-2,4,6-triamine as an organic molecule.

The synthesis process involves slow evaporation. We will discuss the outcomes of the structural analysis using various techniques, involving X-ray diffraction analysis, X-ray powder examination, SEM/EDX, Hirshfield surfaces investigation, vibrational spectroscopy (FT-IR and Raman), thermal analysis (TG/DTG/SDTA and DSC), and exploration of electrical and dielectric properties.

2. EXPERIMENTAL SECTION

2.1. Synthesis. In this study, we prepared a new hybrid compound using 1,3,5-triazine-2,4,6-triamine ($C_3H_6N_6$), zinc chloride ($ZnCl_2$), and hydrochloric acid (HCl). Room temperature crystallization via controlled solvent evaporation was applied to synthesize the compound.

Anhydrous $ZnCl_2$ powder was dissolved in distilled water, while anhydrous $C_3H_6N_6$ powder was dissolved in methanol. These solutions were then combined, and HCl was added while continuously stirring with a magnetic stirrer to ensure that all solutes were completely dissolved. The final mixture was allowed to crystallize slowly. After several days of slow evaporation, colorless single crystals were successfully obtained. We determined the chemical formula of the material through chemical analysis, which was further confirmed by refining the crystal structure.

The chemical reaction is as follows:

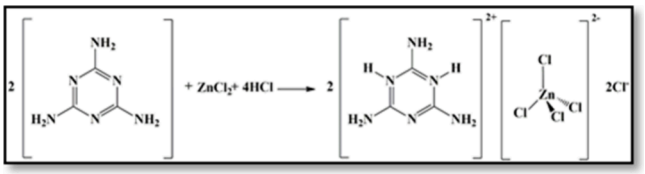

3. INSTRUMENTATION

3.1. X-ray Data Collection. A Bruker Kappa CCD APPEX II diffractometer paired with a Mo Kα radiation source (λ = 0.71073 Å) was applied to gather room temperature X-ray diffraction intensity information needed for the crystal structure across the range of $3.161° \leq \theta \leq 28.489°$. Out of 26,637 reflections recorded, 5,733 met the intensity condition of $I > 2\sigma(I)$. The space group was automatically determined using olex2−1.5,[55] followed by verification of extinction conditions.

A two-step procedure was used to ascertain the crystal structure. An initial resolution was reached by direct approaches, and then Olex2 version 1.5[55] with SHELXL-2018/3[56] software tools were used for refinement.

The structural refinement process encompassed the Full-matrix least-squares refinement on F^2 employing SHELXT program,[57] incorporated atomic coordinates and anisotropic displacement parameters of all non-hydrogen atoms. The hydrogen atoms were placed in geometrically calculated positions and refined by applying fixed isotropic displacement parameters. After several refinement cycles with the olex2−1.5 program,[55] the binding factors obtained were R_1 = 0.050 and wR_2 = 0.104. Figures were generated using the software Diamond 3[58] and ORTEP.[59]

Table 1 displays crystallographic information, as well as details about structural refining. Table S1 shows atomic coordinates and equivalent isotropic displacement settings, whereas Table S2 lists the anisotropic displacement parameters.

Table 1. Main Crystallographic and Structural Refinement Information for Compound $(C_3H_8N_6)_2ZnCl_4{\cdot}2Cl$

Formula	$(C_3H_8N_6)_2ZnCl_4{\cdot}2Cl$
CCDC number	2372132
Formula weight (g mol^{-1})	534.4
Temperature (K)	293
Color	Colorless
Crystal size (mm)	0.2 × 0.13 × 0.1
Crystal system	Monoclinic
Space group	$P2_1/c$
a (Å)	11.7274(3)
b (Å)	6.2155(2)
c (Å)	25.7877(8)
β (deg)	94.27(1)
Volume (Å^3)	1874.50(4)
Z	4
ρ_{cal}	1.894
μ (mm^{-1})	2.19
$\theta_{min}/\theta_{max}$ (deg)	3.161/28.489
hkl	$-16 \leq h \leq 17$
	$-8 \leq k \leq 9$
	$-37 \leq l \leq 35$
Diffractometer	Kappa CCD
λ(Mo Kα) (Å)	λ = 0.71073
Scan mode	$\omega/2\theta$
$F(000)$	1072
Measured reflections	26637
Observed reflections ($I > 2\sigma(I)$)	5733
Number of Refined Parameters	226
$\Delta\rho_{min}/\Delta\rho_{max}$	−0.44/1.23
R_1 [$F^2 > 2\sigma(F^2)$]	0.050
$wR_2(F^2)$[a]	0.104
GooF[b]	0.941

[a] $w = 1/[\sigma 2(F_o^2) + (0.0396P)^2 + 0.6626P]$ or $P = (F_o^2 + 2F_c^2)/3$; $wR = (\sum [w(F_o^2 - F_c^2)^2]/[w(F_o^2)^2])^{1/2}$ and $R = \sum ||F_o| - |F_c||/(\sum |F_o|$

[b] $\text{GooF} = S = \{[w(F^2 - F^2)^2]/(n - p)\}^{1/2}$

3.2. X-ray Powder Diffraction (PXRD). PXRD was performed with an XPERT-PRO powder diffractometer applying Cu Kα radiation (1.54056 Å) in a 2θ range of 5−50° to validate the purity of the produced material. Simulations of PXRD spectra were performed using the programs "Single Crystal Data" and "WINTLOTR".[60]

3.3. Micrographs and X-ray Microanalysis. Scanning electron microscopy analysis was conducted by using a JEOL 6610LV instrument, which included an integrated EDX (Energy Dispersive X-ray) visualization system. To decrease background noise, the instrument's X-ray detector is cooled using liquid nitrogen.

https://doi.org/10.1021/acsomega.4c06685
ACS Omega 2024, 9, 47597−47612

3.4. Hirshfeld Surfaces Methods. The Hirshfeld surfaces[61,62] and their corresponding 2D fingerprints were computed using Crystal Explorer (Version 3.0).[63] The structure input file was supplied in a CIF format. These surfaces offer a visual representation of the spatial relationships between neighboring atoms from interacting molecules.[53]

The calculation of normalized contact distances (d_{norm}) involves the external distance (d_e) measured from the Hirshfeld surface to the closest nucleus outside the surface, the internal distance (d_i) calculated from the Hirshfeld surface to the nearest nucleus inside the surface, and the van der Waals (vdW) radii. These characteristics are used to determine the closeness of intermolecular interactions concerning the sum of van der Waals radii.

The calculation for d_{norm}[62] is given by the following equation:

$$d_{norm} = \frac{d_i - r_i^{vdw}}{r_i^{vdw}} + \frac{d_e - r_e^{vdw}}{r_e^{vdw}}$$

where r_i^{vdw}/r_e^{vdw} denote the van der Waals radius of the atoms inside/outside the surface, respectively.[62]

When d_{norm} was applied to the Hirshfeld surface analysis, three distinct color domains were observed: blue, red, and white. These colors signify the proximity of intermolecular interactions within the crystal structure.

Red areas indicate connections shorter than the sum of van der Waals radii, characterized by negative d_{norm} worth. Blue patches represent connections longer than the total van der Waals radii associated with positive d_{norm} values. However, white regions signify contacts at the van der Waals distance and correspond to d_{norm} values of zero.[64]

A two-fingerprint plot, combining d_e and d_i values, provides a comprehensive overview of these intermolecular contacts.[65,66] Each point on the Hirshfeld surface correlates with specific values of d_i and d_e. A color gradient from blue to green to red demonstrates the density of dots in precise area of the map.

3.5. Spectroscopic Measurements. The vibrational analyses were performed at ambient temperature. The infrared absorption spectra was acquired utilizing a PerkinElmer FT-IR spectrometer, covering the region of 4000−400 cm^{-1}. Similarly, the Raman spectrum was obtained with a Horiba Jobin Yvon LabRAM HR 800 Dual Spectrophotometer ranging from 50 to 4000 cm^{-1}.

3.6. Thermal Characterization. A Mettler Toledo TGA/SDTA851ELF equipment was applied to perform thermal analysis in a dynamic nitrogen environment. The powder sample (15.151 mg) was heated at a rate of 10 K/min between 330 and 980 K.

A SETARAM DSC131 Ks apparatus was used to conduct differential scanning calorimetry (DSC) experiments. The compound was heated between 330 and 800 K, with a sample mass of 2.495 mg. For this experiment, the heating rate was set at 10 K/min in an oxygen atmosphere.

3.7. Electrical Measurements. The electrical characteristic of the studied sample was tested with a two-electrode arrangement. The sample was compressed into pellets (8 mm in diameter and 2 mm thick). Impedance measurements occurred across the frequency range 20 Hz to 10 MHz using the TEGAM 3550 ALF automated bridge, connected to a microcomputer, at temperatures between 313 and 403 K.

4. RESULTS AND DISCUSSION

4.1. Structure Description. The morphology of $(C_3H_8N_6)_2ZnCl_4{\cdot}2Cl$ crystals, as observed via scanning electron microscopy (SEM), is depicted in Figure 1(a). The compound

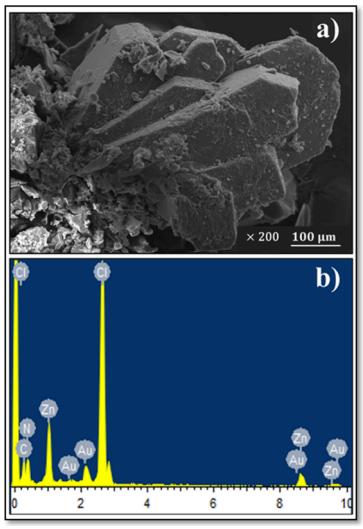

Figure 1. Crystal morphology and scanning electron microscopy (a) and a typical EDX spectrum (b) of $(C_3H_8N_6)_2ZnCl_4{\cdot}2Cl$.

displays crystal fragments that are consistently dispersed with regular edges and smooth surfaces, indicating an excellent level of crystalline quality. The EDX analysis (Figure 1b) confirmed the presence of zinc, chloride, carbon, nitrogen, and oxygen elements, excluding hydrogen, in the growing crystals.

The purity of the synthesized compound $(C_3H_8N_6)_2ZnCl_4{\cdot}2Cl$ was controlled by comparing its powder X-ray diffraction (PXRD) pattern to a simulated pattern recorded from single crystal data (Figure 2). The straight match between the experimental and simulated patterns reveals that the examined compound has a great crystalline purity.

Single-crystal X-ray diffraction was utilized to identify the molecular structure, which demonstrates that the title compound crystallizes in the monoclinic system, specifically in space group $P2_1/c$. The unit cell parameters were: a = 11.7274(3) Å, b = 6.2155(2) Å, c = 25.7877(8) Å, and β = 94.27(1)°, with a volume of V = 1874.50(4) $Å^3$ and containing 4

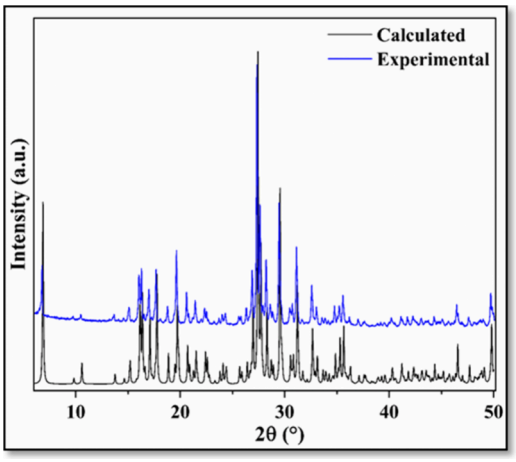

Figure 2. Simulated and experimental XRD of $(C_3H_8N_6)_2ZnCl_4{\cdot}2Cl$.

https://doi.org/10.1021/acsomega.4c06685
ACS Omega 2024, 9, 47597−47612

formula units (Z = 4). The asymmetric unit consists of two deprotonated organic groups $(C_3H_8N_6)^{2+}$, a tetrahedral anion $[ZnCl_4]^{2-}$, and two free chloride ions (Cl^-) to stabilize the crystal structure (Figure 3).

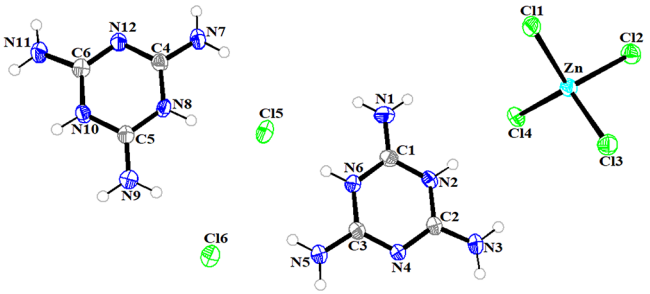

Figure 3. ORTEP presentation of the asymmetric compound unit $(C_3H_8N_6)_2ZnCl_4{\cdot}2Cl$.

A projection onto the (c, a) plane verifies that the crystal structure reveals a layered arrangement consisting of alternative layers of cationic $(C_3H_8N_6)^{2+}$, anionic $[ZnCl_4]^{2-}$ tetrahedra, and isolated chlorine atoms interspersed between the organic molecules to maintain structural stability (Figure 4). The inorganic component features a zinc atom coordinated by four chlorine atoms, forming a tetrahedral coordination (Figure 5(a)).

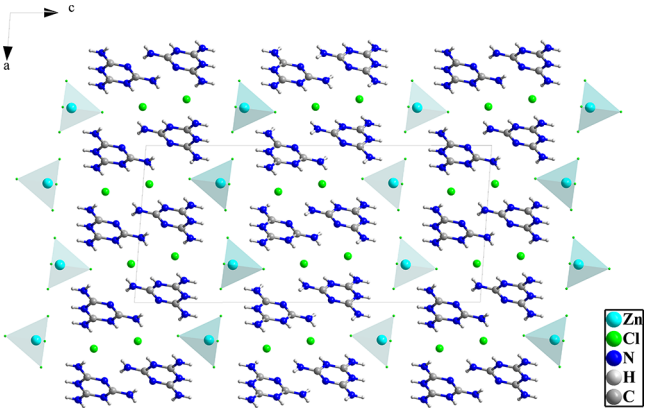

Figure 4. Projection of the compound structure $(C_3H_8N_6)_2ZnCl_4{\cdot}2Cl$ in the plane (c, a).

The Zn−Cl bond lengths in the structure vary from 2.2390(9) to 2.3245(8) Å, spanning a range of 0.0855 Å. Chlorine atoms (Cl_2, Cl_3, Cl_4), involved in hydrogen bonding, possess the longest Zn−Cl distances.

The Cl−Zn−Cl bond angles in the structure vary from 105.76(3)° to 116.43(3)°. Mean distortion indices for bond angles and distances within the $[ZnCl_4]^{2-}$ tetrahedron were calculated using the method declared by Baur.[67]

$$DI(Zn{-}Cl) = \frac{\sum |ZnCl_i - ZnCl_m|}{4ZnCl_m}$$

$$DI(Cl{-}Zn{-}Cl) = \frac{\sum |Cl_iZnCl_i - Cl_mZnCl_m|}{6Cl_mZnCl_m}$$

$$\Delta_{tetra} = \frac{1}{4}\sum\left(\frac{ZnCl_i - ZnCl_m}{ZnCl_m}\right)^2$$

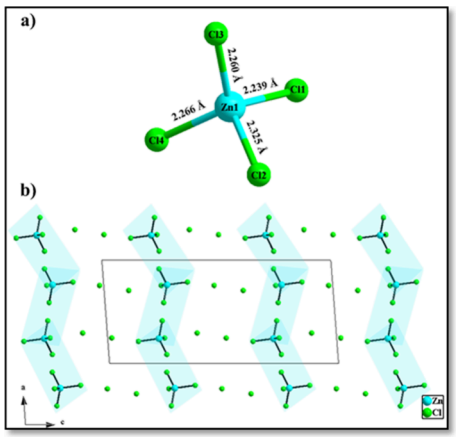

Figure 5. (a) Geometry of the inorganic group and (b) projection of the inorganic entity of the compound $(C_3H_8N_6)_2ZnCl_4{\cdot}2Cl$ in the (c, a) plane.

with Zn−Cl_i: distance between zinc and chlorine in the $ZnCl_4$ tetrahedron, Zn−Cl_m: average distance between zinc and chlorine in the $ZnCl_4$ tetrahedron, Cl_i−Zn−Cl_i: angle, Cl_m−Zn−Cl_m: average angle.

The distortion indices for the $ZnCl_4$ tetrahedra provide insight into their geometric configuration. The calculated values are DI (Zn−Cl) = 33.10^{-4}, DI (Cl−Zn−Cl) = 3.10^{-5}, and Δ_{tetra} = 0. These values suggest that the $ZnCl_4$ tetrahedra displays slight distortion from ideal tetrahedral geometry.[68]

The crystal structure analysis reveals that the hybrid compound $(C_6H_{18}N_3)[ZnCl_4]Cl$ crystallizes in the monoclinic system, occupying the space group $P2_1$.[69]

This compound shares the same inorganic component as the title compound. However, substituting the cationic part with a different organic molecule influences the structural properties of the synthesized materials.

The material under study differs from the compound $(C_6H_{18}N_3)[ZnCl_4]Cl$,[69] in terms of crystallographic symmetry. While both materials crystallize in the monoclinic system, there is a significant difference in the space group. The compound $(C_6H_{18}N_3)[ZnCl_4]Cl$ adopts the noncentrosymmetric space group $P2_1$, whereas the new material crystallizes in the centrosymmetric space group $P2_1/c$. This change demonstrates an increase in symmetry with the introduction of a center of inversion in the investigated crystal structure.

An examination of the crystal structure of the compound $(C_6H_{18}N_3)[ZnCl_4]Cl$[69] demonstates that the zinc-chlorine bond lengths in the tetrachlorozincate anion $[ZnCl_4]^{2-}$ vary between approximately 2.2582(4) and 2.2813(5) Å. In addition, the angles formed by chlorine atoms surrounding the central zinc atom in this anion range from about 104.667(16)° to 112.083(16)°.

The $[ZnCl_4]^{2-}$ tetrahedron's angles and bonds provide mean distortion values of DI (Zn−Cl) = 38.10^{-4}, DI (Cl−Zn−Cl) = 25.10^{-3}, and Δ_{tetra} = 0, indicating a distorted tetrahedral coordination geometry. Consequently, the coordination geometry of the Zn atom in the new compound is a less distorted tetrahedron compared to $(C_6H_{18}N_3)[ZnCl_4]Cl$,[69] may be due to differences in ligand size, charge, or metal−ligand bond strength.

In $(C_6H_{18}N_3)[ZnCl_4]Cl$,[69] N−H···Cl and C−H···Cl hydrogen bonds hold the structure together. In contrast, the title compound's stability is maintained through N−H···Cl and N−

https://doi.org/10.1021/acsomega.4c06685
ACS Omega 2024, 9, 47597−47612

H···N hydrogen bonds. These distinctions in hydrogen bonding patterns can be related to differences in the organic parts and the number of free chloride ions present in each structure.

$(C_3H_8N_6)_2ZnCl_4{\cdot}2Cl$ features a zigzag sequence of isolated tetrahedra along the *a*-axis (Figure 5(b)). Examining the crystal structure along the *c*-axis presents layers of $ZnCl_4$ tetrahedra at fractional coordinates $z = 1/4$ and $3/4$. Between these layers of tetrahedral anions, two isolated chloride ions are positioned.

Figure 6(a) illustrates the arrangement of cations in the (*c*, *a*) plane, forming layers perpendicular to the *c*-axis. The aromatic

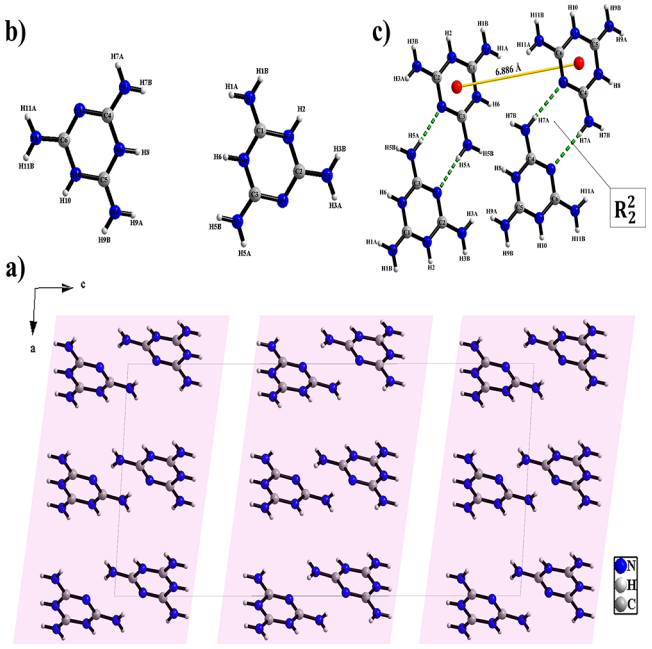

Figure 6. (a) Representation of the compound's organic portion projected onto the ac plane, (b) Geometry of the organic grouping and (c) $\pi-\pi$ interaction of the compound $(C_3H_8N_6)_2ZnCl_4{\cdot}2Cl$.

nuclei align parallel to each other. The $C_3H_8N_6$ group has two protonated nitrogen ring sites, converting neutral $C_3H_6N_6$ into a diprotonated $(C_3H_8N_6)^{2+}$ group (Figure 6(b)).

The nitrogen−carbon bond lengths in the organic cations range between approximately 1.298(4) and 1.372(4) Å. Conversely, the N−H distances are found to be 0.86 Å. N−C−N angles range from 116.5(3)° to 122.5(3)°. C−N−C angles range from 116.4(3)° to 121.6(3)°, C−N−H angles range from 119.7° to 120°, and N−H−N angles are 120°. These values are similar to those of the $C_3H_8N_6$ group in the $[H_2mela]_2PbCl_5$. Cl compound previously documented.[51] In the latter material, the molecular geometry of the organic component features N−C bond lengths ranging from approximately 1.299(4) to 1.367(4) Å. The N−C−N bond angles span from about 116.9(3)° to 122.4(3)°, while the C−N−C bond angles vary from roughly 116.7(2)° to 121.4(2)° (Table S3). The cations are symmetrically arranged in pairs between the centroids of two aromatic rings, with an average distance of 6.886 Å (>3.8 Å), indicating the absence of $\pi-\pi$ interactions (Figure 6(c)).[70,71] The connection between two organic cations $(C_3H_8N_6)^{2+}$ forms a binary ring of type $R^2_2(8)$[72] (Figure 6(c)) through N−H···N hydrogen bonds. Both N−H···Cl and N−H···N hydrogen bonds ensure the crystalline structure's stability within $(C_3H_8N_6)_2ZnCl_4{\cdot}2Cl$.

4.1.1. Cation−Anion Bonds. The molecules within the crystal are linked because of the N−H···Cl hydrogen bonding (Figure 7(a)), detailed in Table 2. relating to Brown's criteria for

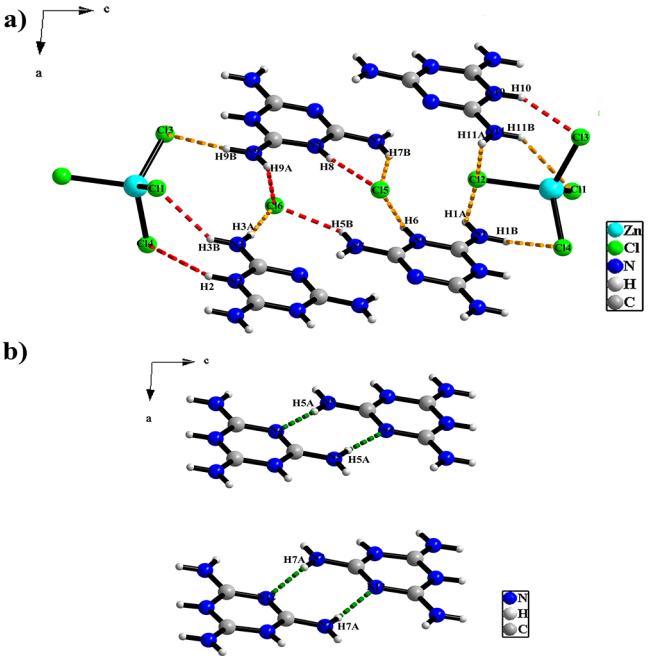

Figure 7. (a) N−H···Cl Hydrogen bonding and (b) N−H···N hydrogen bonds of compound $(C_3H_8N_6)_2ZnCl_4{\cdot}2Cl$.

Table 2. Characteristic Lengths and Angles of H-Bonds in $(C_3H_8N_6)_2ZnCl_4{\cdot}2Cl$

D−H···A[a]	D−H	H···A	D···A	D−H···A
N1−H1A···Cl2^{i}	0.86	2.74	3.4640(1)	143
N1−H1B···Cl4^{i}	0.86	2.54	3.2528(1)	141
N2−H2···Cl4^{vi}	0.86	2.31	3.1247(1)	158
N3−H3A···Cl6	0.86	2.41	3.2569(1)	169
N3−H3B···Cl1^{ii}	0.86	2.48	3.1873(1)	140
N5−H5A···N4^{vii}	0.86	2.14	3.9990(1)	176
N5−H5B···Cl6^{vii}	0.86	2.38	3.0887(1)	140
N6−H6···Cl5^{i}	0.86	2.13	3.9796(1)	171
N7−H7A···N12^{iii}	0.86	2.40	3.2562(1)	172
N7−H7B···Cl5^{viii}	0.86	2.64	3.3696(1)	144
N8−H8···Cl5^{viii}	0.86	2.17	3.0033(1)	164
N9−H9A···Cl6^{iv}	0.86	2.38	3.1754(1)	155
N9−H9B···Cl3^{i}	0.86	2.54	3.3014(1)	148
N10−H10···Cl3^{ix}	0.86	2.35	3.1326(1)	151
N11−H11A···Cl2^{v}	0.86	2.47	3.2751(1)	157
N11−H11B···Cl1^{v}	0.86	2.57	3.2097(1)	132

[a]Symmetry codes: (i) *x*, −1 + *y*, *z*; (ii) 1 − *x*, 1/2 + *y*, 1/2-*z*; (iii) −*z*, 1 − *y*, 1 − *z*; (iv) 1 − *z*, −3/2 + *y*, 1/2 − *z*; (v) −*z*, 1/2 + *y*,1/2 − *z*; (vi) 1 − *z*, −1/2 + *y*, 1/2 − *z*; (vii) 1 − *z*, 1 − *y*, −*z*; (viii) *x*, 1/2 − *y*, 1/2 + *z*; (ix) −*z*, −1/2 + *y*,1/2 − *z*.

distances D···A,[73] six distances are marked as strong-character hydrogen bonds (dashed red lines), characterized by N···Cl distances between approximately 3.0033(1) and 3.1873(1) Å. Eight distances are attributed weak-character hydrogen bonds (dashed orange lines), with N···Cl distances spanning from about 3.2097(1) to 3.4640(1) Å.

4.1.2. Cation−Cation Bonds. The crystalline structure is also stabilized by two N−H···N intermolecular bonds (Figure 7(b)),

https://doi.org/10.1021/acsomega.4c06685
ACS Omega 2024, 9, 47597−47612

with N···N distances varying between approximately 3.2562(1) and 3.9990(1) Å. The angles and lengths that characterize the hydrogen bonds can be found in Table 2.

Comparing with a similar previous material $(C_7H_{16}N_2)$-$ZnCl_4$,[74] the hydrogen bonds in the title compound are stronger. In the previous study, the intermolecular interactions are limited to N−H···Cl hydrogen bonds. These bonds are characterized as weak, with N···Cl distances spanning approximately 3.22−3.58 Å. However, there is one strong-character hydrogen bond with a N···Cl distance of 3.157(3) Å. The differences in hydrogen bonding between this material and the examined compound can be related to variations in the organic part and the presence of two free chlorine atoms in the title compound.

4.2. Hirshfeld Surface Investigation. To clarify the character and importance of intermolecular contact inside the synthesized crystal structure, Hirshfeld surface investigation was reported.

Figure 8(a-e) illustrates the Hirshfeld surfaces characterized by various parameters. The d_{norm} values range from 0.4955 to

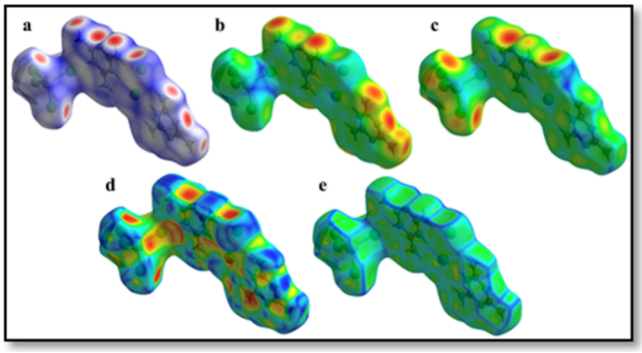

Figure 8. Hirshfeld surface mapped d_{norm} (a), d_i (b), d_e (c), shape index (d), and curvedness (e).

1.0082 Å, while d_i and d_e span from 0.8018 to 2.6408 Å and 0.8031 to 2.6212 Å, respectively. The shape index, in Å, varies between −1.000 and 1.000, and the curvedness extends from −4.000 to 0.400. The red spots on the d_{norm} surface prove the presence of N−H···Cl and N−H···N hydrogen bonding. Furthermore, other visible points originate from the H···H contacts.

Considering the nearest neighbors both inside and outside, the 3D nanoresolved surface may be resolved into 2D fingerprint drawings. This analytical approach enables the differentiation and quantification of distinct intermolecular interactions that are collectively represented in a complete fingerprint plot. Figure 9 illustrates the resulting fingerprint regions.

The percentages of the area occupied by different interactions in $(C_3H_8N_6)_2ZnCl_4{\cdot}2Cl$ are presented in Figure 10. These surfaces have been fingerprinted with plots showing a d_i of 1.7540 Å and a d_e of 1.7448 Å.

For the title compound, H···Cl/Cl···H and N···H/H···N contacts are the most prevalent interactions, with their relative contributions reaching 46% and 16.8%, respectively, representing N−H···Cl and N−H···N H-bond contacts. These results are confirmed by the structural study (Table 2).

According to the fingerprint map examination, H···H interactions are the third predominant interaction, accounting for 13.5% of the total Hirshfeld surface area. This is related to the important presence of hydrogen on the compound's surface. This electrostatic interaction ensured the stability of the

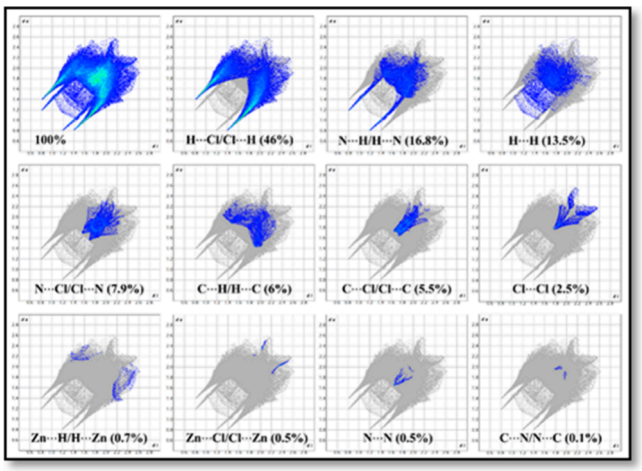

Figure 9. Fingerprint analysis of the compound.

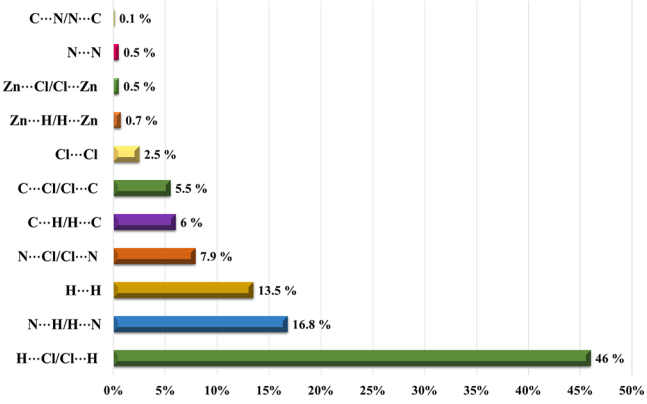

Figure 10. Distribution of intermolecular contacts on the Hirshfeld surface of $(C_3H_8N_6)_2ZnCl_4{\cdot}2Cl$.

structure. In addition other interactions with low percentages that may be considerate negligible (Figure 10).

4.3. Infrared and Raman Spectra. By comparing the infrared and Raman spectra of $(C_3H_8N_6)_2ZnCl_4{\cdot}2Cl$ at ambient temperature with those of various compounds linked to comparable anions or adjacent cations in previous studies, the compound's molecular structure is confirmed.

The IR and Raman spectra of the compound under study are presented in Figures 11 and 12, respectively. The IR spectrum spans the wavenumber range 550−3750 cm^{-1}. However, the Raman spectrum covers a broader range of 50−3750 cm^{-1}.

Table 3 presents the assignments of the recorded vibrations. In the high-frequency domain, peaks observed at 3700, 3592, 3476, 3464, and 3446 cm^{-1}, in the Raman spectrum, are associated with the elongation vibration modes ν (N−H).[44,54]

The peak that appears at 3322 cm^{-1} in IR and at 3393 cm^{-1}, in the Raman spectrum, can be associated with the symmetrical elongation vibration ν_s (NH_2).[47,75] The elongation vibration mode ν (N−H) is observed, in the IR, in the range of 2949- 2744 cm^{-1} and in the Raman spectrum in the range of 2806−2623 cm^{-1}.[47,75,76]

A low peak observed at 1648 cm^{-1}, in the IR, and at 1722 and 1684 cm^{-1}, in the Raman, is credited to the deformation vibration δ (N−H).[51,77,78] In the IR spectrum, the deformation vibration δ (NH_2) appears as a small band at 1616 cm^{-1}.[24] Symmetrical bending in the β_s plane (NH_2) is localized in IR around 1594 cm^{-1} and in Raman around 1598 cm^{-1}.[75]

https://doi.org/10.1021/acsomega.4c06685
ACS Omega 2024, 9, 47597−47612

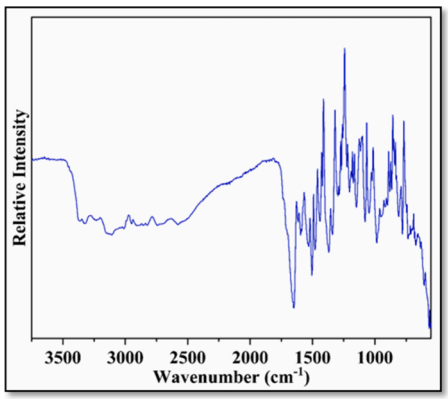

Figure 11. FT-IR spectra of $(C_3H_8N_6)_2ZnCl_4{\cdot}2Cl$.

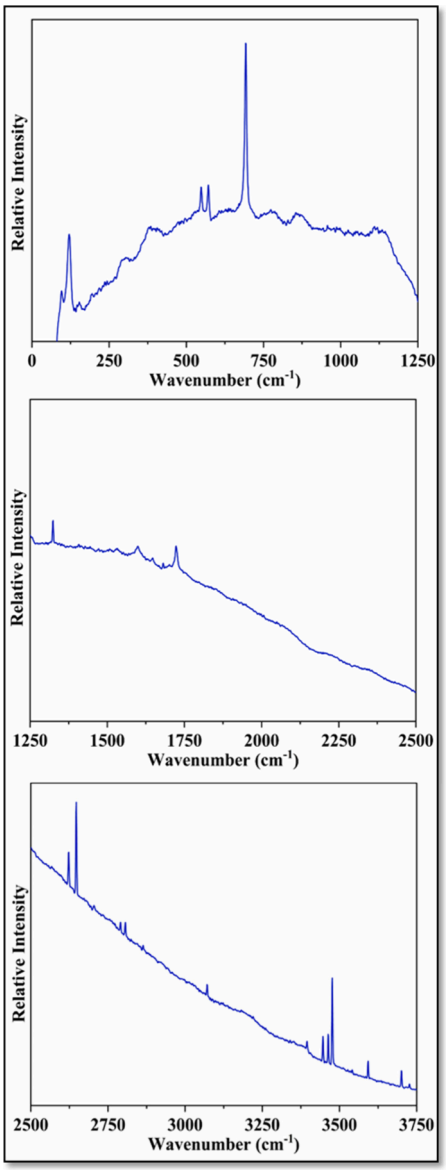

Figure 12. Raman spectra at room temperature of $(C_3H_8N_6)_2ZnCl_4{\cdot}2Cl$.

The two main bands observed in IR at 1530 and 1505 cm^{-1} can be ascribed to the asymmetric elongation vibration of the lateral groups ν_{as} (C−N).[50,75] Additionally, the low peaks that appear at 1479, 1440, and 1420 cm^{-1} in IR and at 1109 cm^{-1} in Raman are associated to the elongation vibrations ν (C−N).[47,49,77] The main band at 1368 cm^{-1} in IR can be attributed to the elongation vibration of the ring ν (C═N) of the aromatic nucleus.[50,79]

The weak bands observed only in the IR spectrum between 1339 and 1209 cm^{-1} can be linked to the ring torsion vibration τ (NH_2).[24] In contrast, the δ (N−C−NH_2) deformation vibration appears only in Raman at 1324 cm^{-1}.[61]

Deformation in the rocking ρ (NH_2) plane is observed in IR in the range of 1186−1021 cm^{-1} and in Raman at 1025 cm^{-1}.[47,75] The peak that appears at 985 cm^{-1} in IR is assigned to the vibration of the triazine ring.[47,50,51,76] Asymmetric ν_{as} (C−N) elongation vibrations are observed in IR spectrum at 952 cm^{-1} and in Raman spectrum at 957 cm^{-1}.[80] Symmetric ν_s (C−N) elongation vibrations are observed, in the IR, between 917 and 865 cm^{-1} and in Raman at 863 cm^{-1}.[81]

Peaks observed, in the IR, at 851, 841, and 829 cm^{-1} and in Raman at 854 cm^{-1} are attributed to δ (C−N−C) deformations of the aromatic nucleus.[74] The deformation vibration modes γ (C−N−C) in the studied organic molecule are observed at 809, 779, and 745 cm^{-1} in IR and at 791 and 773 cm^{-1} in the Raman spectrum.[47,51,76] An intense peak that appears at 693 cm^{-1} in Raman and two weak peaks that appear at 683 and 671 cm^{-1} in IR can be attributed to the out-of-plane vibration γ (N−C−N) of the aromatic nucleus.[47,51,75]

Table 3. Band Assignments and Reported Infrared and Raman Frequencies (cm^{-1}) at Ambient Temperature for $(C_3H_8N_6)_2ZnCl_4{\cdot}2Cl$[a]

IR (cm^{-1})	Raman (cm^{-1})	Assignments
	3700/3592/3476/3464/3446	ν (N−H)
3322	3393	ν_s (NH_2)
2949−2744	2806−2623	ν (N−H)
1648	1722/1648	δ (N−H)
1616		δ (NH_2)
1594	1598	β_s (NH_2)
1530/1505		ν_{as} (C−N)
1479/1440/1420		ν (C−N)
1368		ν (C═N)
1339−1209		τ (NH_2)
	1324	δ (N−C−NH_2)
	1109	ν (C−N)
1186−1021	1025	ρ (NH_2)
985		Vibration of the triazine ring
952	957	ν_{as} (C−N)
917−865	863	ν_s (C−N)
851/841/829	854	δ (C−N−C)
809/779/745	791/773	γ (C−N−C)
683/671	693	γ (N−C−N)
565	571/547	β (C−N−C)
	495	β (N−C−N)
	473	δ_{as} (C−N)
	405	δ_s (C−N)
	217	ν_{as} (Zn−Cl)
	194	ν_s (Zn−Cl)
	120	δ_{as} (Cl−Zn−Cl)
	95	δ_s (Cl−Zn−Cl)

[a]Abbreviations: ν: elongation, δ: deformation, β: bending in plane, γ: bending out of plane, ρ: roking, τ: ring torsion (out of plane), as asymmetric, s: symmetric.

https://doi.org/10.1021/acsomega.4c06685
ACS Omega 2024, 9, 47597−47612

The two main peaks observed at 571 and 547 cm^{-1} in Raman and the main band observed at 565 cm^{-1} in IR are associated with the bending vibration modes in the plane β (C−N−C).[47,51] The bending vibration in the plane β (N−C−N) is evidenced in Raman at about 495 cm^{-1}.[47,51,76] The two weak peaks at 473 and 405 cm^{-1} in Raman are assigned to both asymmetric and symmetric deformation vibrations of the C−N group.[82] The modes of vibration of the anionic group $[ZnCl_4]^{2-}$ are observed only in Raman at 400 cm^{-1}.

External modes are observed in Raman at low frequencies. Indeed, in this spectrum, two peaks of low intensities at 217 and 194 cm^{-1} correspond to the asymmetric and symmetrical elongation vibrations ($\nu_{as/s}$ (Zn−Cl)), respectively.[79] Additionally, the vibrations of the asymmetric and symmetric deformations (δ_{as} (Cl−Zn−Cl) and δ_s (Cl−Zn−Cl)) in the anion $[ZnCl_4]^{2-}$ appear at 120 and 95 cm^{-1}, respectively.[47]

4.4. Thermal Behavior. The thermal analysis findings for $(C_3H_8N_6)_2ZnCl_4{\cdot}2Cl$, acquired by concurrent TG/DTG and SDTA measurements, are shown in Figure 13. Furthermore, Figure 14 displays the differential scanning calorimetry (DSC) curve.

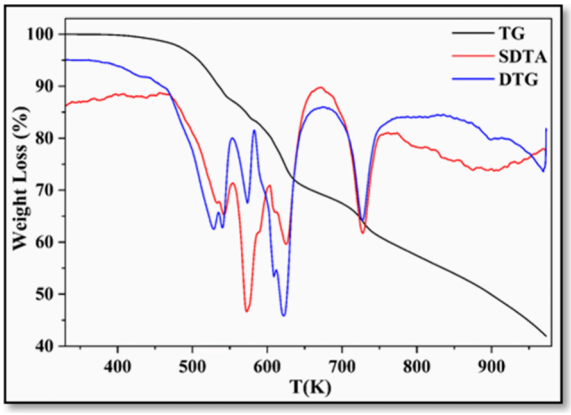

Figure 13. TG-DTG-SDTA curves for $(C_3H_8N_6)_2ZnCl_4{\cdot}2Cl$.

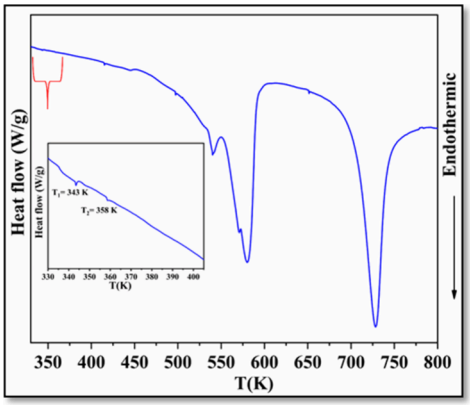

Figure 14. DSC thermogram of the $(C_3H_8N_6)_2ZnCl_4{\cdot}2Cl$ compound.

The TG thermogram indicates that the investigated material remains stable up to 405 K. The DSC thermogram displays two anomalies during heating at temperatures of T_1 = 343 K and T_2 = 358 K (Figure 13). These anomalies, observed within the material's thermal stability region, are likely attributed to phase transitions. The phase transition at T_2 is expected to be order−disorder related.[83]

The thermogravimetric (TG) curve of the title compound shows a total weight loss of 58.04% (calculated: 57.25%). The TG/DTG curves (Figure 13) indicate that the compound decomposes in five sequential mass losses. The $(C_3H_8N_6)_2ZnCl_4{\cdot}2Cl$ material releases four chlorine atoms as HCl during the evolution of the TG thermogram in the temperature range from 405 to 637 K (Figure 13). Five successive endothermic peaks in the DTG curve between 528 and 621 K, six successive endothermic peaks between 528 and 625 K in the SDTA curve and between 415 and 580 K in the DSC graph (Figures 13 and 14) confirm that the first mass loss is a combination of three sequential losses amounting to 27.98% (calculated: 26.29%).

The second mass loss is a combination of two sequential losses occurring between 637 and 972 K. The experimental weight loss is 30.05% whereas the calculated one is 29.97%. This is correlated with an endothermic peak at 728 K in the DTG/SDTA and DSC curves. This loss is associated with the decomposition of the organic molecules, corresponding to the decomposition of two molecules of $(C_3H_2N_3)$. According to the analysis and calculations, the remaining products after decomposition are $ZnCl_2$ and five molecules of NH_3 gases (experimental mass loss: 41.96%, theoretical mass loss: 41.43%).

The compound $(C_3H_8N_6)Cu_2Cl_6$[49] has two endothermic peaks at 338 and 488 K, associated with a phase transition and the compound's melting, respectively. The fusion temperature of the new compound is 728 K, which is higher than the fusion temperature of $(C_3H_8N_6)Cu_2Cl_6$,[49] which is 488 K. This suggests that the cations in the new compound have stronger hydrogen bonds than those in $(C_3H_8N_6)Cu_2Cl_6$, resulting in higher thermal stability for the new compound compared to $(C_3H_8N_6)Cu_2Cl_6$.

4.5. Electrical Properties. *4.5.1. Impedance Measurements and Equivalent Circuit Representation.* The electrical characteristics of dielectric compounds may be examined by using complex impedance spectroscopy across a defined frequency range. Applying this technique, the effects from different phenomena, including grain characteristics, grain boundary phenomena, and electrode-material interfacial interactions, may be separated and examined.[53] For this analysis, complex impedance measurements ($Z^* = Z' - jZ''$) were taken within the temperature range of 313−403 K, as seen in Figure 15. The measurements of impedance (Z^*), electric modulus (M^*), permittivity (ε^*), and admittance (Y^*) are interconnected, providing a comprehensive understanding of the compound's electrical behavior.

Both the imaginary (Z'') and real (Z') components of the complex impedance are useful for understanding the dielectric features and their variation with frequency and temperature. By analyzing these components, it is possible to distinguish between different types of polarization and conduction mechanisms within the material. The complex impedance spectroscopy approach is particularly useful in separating contributions from grain and grain boundary effects as well as the electrode-material interface.

In addition, the study of the electric modulus (M^*), which corresponds to the reciprocal of permittivity, helps to identify relaxation processes within the material. The electric modulus can provide information about the conductivity relaxation and the mobility of the charge carriers. Similarly, the admittance (Y^*), the inverse of impedance, offers essential insight into the material's conductive features.

https://doi.org/10.1021/acsomega.4c06685
ACS Omega 2024, 9, 47597−47612

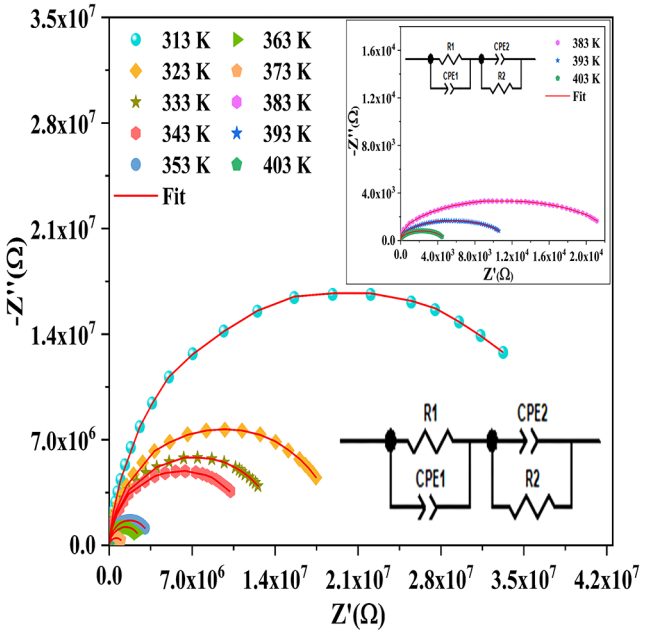

Figure 15. Nyquist diagram spectra plotted against temperature and the corresponding electrical equivalent circuit for $(C_3H_8N_6)_2ZnCl_4{\cdot}2Cl$.

Furthermore, the interconnected nature of these measurements allows for a detailed study of the dielectric properties and the underlying mechanisms influencing the electrical behavior of $(C_3H_8N_6)_2ZnCl_4{\cdot}2Cl$ within the examined temperature range.

$$M^* = j\omega C_0 Z_0$$

$$\varepsilon^* = (M^*)^{-1}$$

$$Y^* = (Z^*)^{-1}$$

$$Y^* = j\omega C_0 \varepsilon^*$$

The diagram in Figure 15 presents the Nyquist plots of the compound under study obtained at various temperatures.

In contrast to the ideal semicircular plot aligned with the real axis, the plot shows some dispersion, demonstrating Cole−Cole empirical behavior. The semicircle radius diminishes as the temperature rises, leading to a decrease in the resistance. This behavior confirms that the conductivity increases with temperature.[81,84,85] This diagram features semicircles, revealing two contributions.[86] The first is observed in the high-frequency range, presenting the effect of grains, while the second is observed in the low-frequency range, relating to the grain boundaries' impact.

Z-view software was applied to explore impedance data using a standard equivalent circuit model. This circuit consisted of the series connection of two cells with each cell formed by a parallel arrangement of a resistor (R) and a fractal capacitance (CPE) (Figure 15). Here, the impedance of the capacitance at the fractal interface (CPE) is represented by the equation:

$$Z_{CPE} = \frac{1}{Q_0(j\omega)^{\alpha}}$$

where the capacitance value of the CPE element is Q, and the fractal constant is α. The previous calculation shows that ,$Z(\mathrm{CPE}) = 1/jQ\omega$ and if $\alpha = 1$, the CPE contains pure capacitance. In contrast, if $\alpha = 0$, then $Z(\mathrm{CPE}) = 1/Q$ and the CPE has a pure resistance. At different temperatures, Figure 16

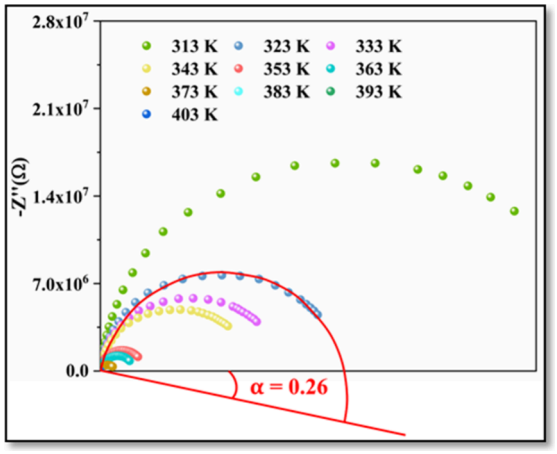

Figure 16. Cole−Cole representation showing the α deviation of Debye's behavior.

demonstrates that $\alpha = 0.26$. To determine the real (Z') and imaginary (Z'') components of the impedance, the following formulas were applied:

$$Z' = \frac{R^{-1} + Q\omega^{\alpha}\cos\left(\frac{\alpha\pi}{2}\right)}{\left(R^{-1} + Q\omega^{\alpha}\cos\left(\frac{\alpha\pi}{2}\right)\right)^2 + \left(C\omega + Q\omega^{\alpha}\sin\left(\frac{\alpha\pi}{2}\right)\right)^2}$$

$$Z'' = \frac{R^{-1} + Q\omega^{\alpha}\sin\left(\frac{\alpha\pi}{2}\right)}{R^{-1} + \left(Q\omega^{\alpha}\cos\left(\frac{\alpha\pi}{2}\right)\right)^2 + C\omega + \left(C\omega^{\alpha}\sin\left(\frac{\alpha\pi}{2}\right)\right)^2}$$

Figure 17(a) provides a graph showing the connection between the real component of impedance (Z') and frequency at various temperatures. At lower temperatures, the Z' amplitude is greater in the low-frequency range, gradually decreasing as both frequency and temperature rise, leading to an increase in the material's AC conductivity. Beyond 5 Hz, all the curves converge, making Z' frequency independent. Additionally, as Z' decreases, the relaxation frequency shifts to a higher frequency.

Figure 17(b) depicts the correlation between the imaginary portion of impedance (Z'') and frequency at various temperatures. As frequency and temperature increase, the magnitude of Z'_{max} decreases. The shift of the Z''_{max} peaks to higher frequencies with increased temperature indicates a relaxation event in the system, suggesting a loss in resistive characteristics.[87] The merging of all curves at high frequencies suggests a potential release of space charge.

Furthermore, the plots in Figure 17(a),(b) demonstrates a significant connection between both theoretical and experimental data, implying that the suggested equivalent circuit effectively represents the pellet-electrolyte interface.

Figure 18 illustrates the changes in Z' and $-Z''$ with varying angular frequency at 343 K. The proposed equivalent circuit demonstrates a good fit between the observed and calculated impedances. Z' decreases with increasing frequency, while $-Z''$ increases, peaking at a specific frequency where it intersects with Z'. Above this frequency, both Z' and $-Z''$ reduce and approach the *x*-axis, suggesting the presence of a relaxation process.[88]

The resistance values (R) resulting from fitting the impedance spectra were utilized to calculate the σ_{dc} conductivity using the relevant formula:

https://doi.org/10.1021/acsomega.4c06685
ACS Omega 2024, 9, 47597−47612

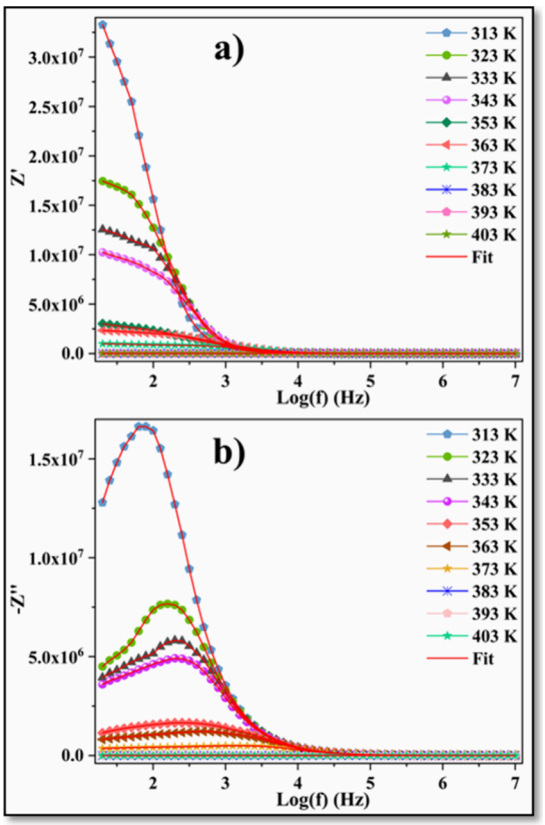

Figure 17. Variation of impedance with frequency for different temperatures; (a) real part Z' and (b) imaginary part $-Z''$.

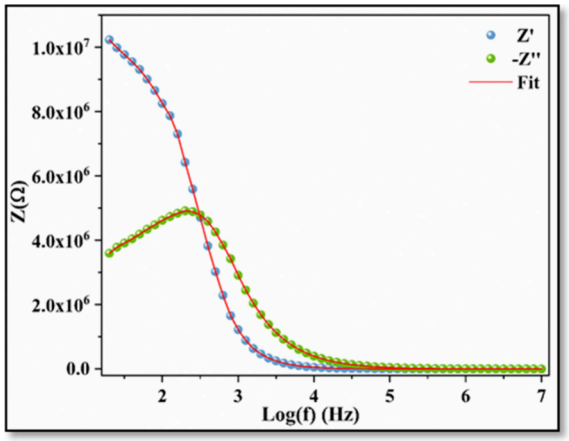

Figure 18. Variation of Z' and $-Z''$ with frequency at 343 K of $(C_3H_8N_6)_2ZnCl_4{\cdot}2Cl$ compound.

$$\sigma_{dc} = \frac{e}{RS}$$

R is the resistance suggested from the impedance spectra fitting, S is the sample area, and e is the sample thickness.

Figure 19 displays the evolution of $\log(\sigma_{dc})$ as a function of $1000/T$. The plot illustrates that the conductivity of the compound rises with temperature, implying that conduction in the compound is regulated by the Arrhenius equation:

$$\sigma_{dc}T = \sigma_0 \exp(-E_a/k_BT)$$

The change in slope at T_1 = 343 K and T_2 = 373 K proves the presence of a conduction phase transition in the studied

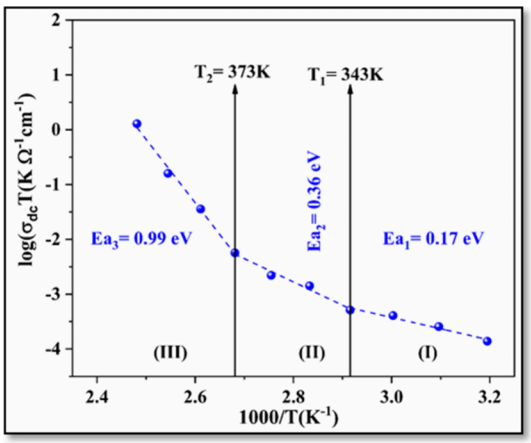

Figure 19. Variation of the $\log(\sigma_{dc})$ versus 1000/T of the $(C_3H_8N_6)_2ZnCl_4{\cdot}2Cl$ compound.

compound, which was further supported by identifying three regions (I), (II) and (III) through the linear fit of the graph's conductivity as shown in Figure 19. The activation energies calculated for regions (I), (II), and (III) are E_{a1} = 0.17 eV, E_{a2} = 0.36 eV, and E_{a3} = 0.99 eV, respectively.

The conductivity curve indicates that the studied compound demonstrates super ionic-protonic conduction phenomena. This behavior is related to the disruption of N−H···Cl and N−H···N hydrogen bonds, along with a substantial restructuring of the crystal lattice resulting from a chemical transformation.[7,53] This leads the proton to oscillate between the potential wells.

The $((C_2H_5)NH_3)_2ZnCl_4$[89] material has the same inorganic part as the title compound and exhibits activation energies of E_a(I) = 0.28 eV, E_a(II) = 1.05 eV, and E_a(III) = 1.03 eV. These activation energies are higher than those of the title compound, suggesting stronger hydrogen bonds in $((C_2H_5)NH_3)_2ZnCl_4$. When the σ_{dc} conductivity of the two compounds is compared, it seems that the synthesized compound has higher conductivity, which correlates with its lower activation energy.

4.5.2. AC Electrical Conductivity. AC conductivity provides valuable insights into the electrical behavior of a material, encompassing conductivity, capacitance, and loss factor dynamics. It aids in discerning the type of conduction present within a sample and is derived from complex impedance data by using specific equations.

$$\sigma_{ac} = \frac{e}{S}\frac{Z'}{Z'^2 + Z''^2}$$

Figure 20 depicts the fluctuation in AC conductivity with frequency at several temperatures. The curves for the examined samples show two distinctive zones.

At low frequencies, the AC conductivity is constant, while at high frequencies, it shows dispersion. Increasing the frequency enhances the hopping frequency of charge carriers, thereby improving the conduction process and resulting in an overall increase in the conductivity. This feature implies a thermally activated process caused by the energy levels of the charge carriers.

At lower frequencies, the applied electric field drives charge carriers to move over longer distances, resulting in decreased charge carrier mobility as the frequency increases.[53,90]

4.6. Dielectric Studies. Dielectric materials are essential in the advancement of sophisticated electronic technologies, providing critical insights into their properties through measure-

https://doi.org/10.1021/acsomega.4c06685
ACS Omega 2024, 9, 47597−47612

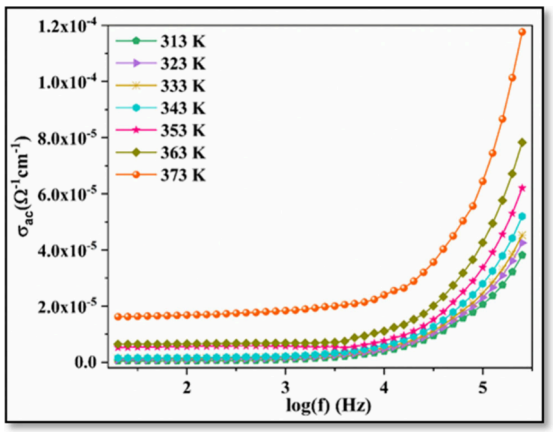

Figure 20. Frequency dependence of AC conductivity at various temperatures.

ments such as dielectric, impedance, and modulus.[53] These materials are pivotal for charge storage applications, prominently in capacitors and in the construction of radio frequency transmission lines. High-permittivity dielectrics are particularly employed to enhance the semiconductor performance. Furthermore, hybrid materials possessing dielectric properties are highly sought after for potential uses in integrated circuits and high-frequency printed circuit boards.[91]

4.6.1. Real and Imaginary Permittivity. The study of dielectric properties offers detailed insights into conduction processes,[92] electrical and dipolar relaxation times, and activation energies.[93] A non-Debye model defines dielectric relaxation by describing the frequency-dependent complex permittivity using the following equation:[94]

$$\varepsilon^* = \varepsilon' - j\varepsilon''$$

The real portion ε' of the dielectric constant suggests the stored energy and is described by the relation: $\varepsilon' = 1/\omega C_0[-Z''/(Z'^2+Z''^2)]$

Figure 21(a) highlights the frequency dependence of the real component of the dielectric constant. It shows a decrease in the dielectric constant as the frequency increases, with a tendency to stabilize at higher frequencies across all temperatures. The pronounced variation of ε' at lower frequencies indicates significant conductivity contributions in the material. The high ε' values at low frequencies are likely due to lattice vibrations and macroscopic distortions in the crystal structure, while the lower values at higher frequencies suggest a gradual attenuation of these vibrations.

The following relation is utilized to define the imaginary portion ε'' of the dielectric constant, which specifies the dissipated energy:

$$\varepsilon'' = \frac{1}{\omega C_0}\left[\frac{-Z'}{Z'^2 + Z''^2}\right]$$

The dielectric constant ε' (Figure 21(a)) and the dielectric loss ε'' as a function of temperature and frequency (Figure 21(b)) vary similarly. The dielectric constants at low frequencies have a dispersive tendency as the temperature increases. Non-Debye dependence is confirmed by the significant increase in dielectric loss, which verifies the presence of electrode polarization and space charge impacts.[95] As demonstrated, no significant relaxation peaks were detected in the frequency range

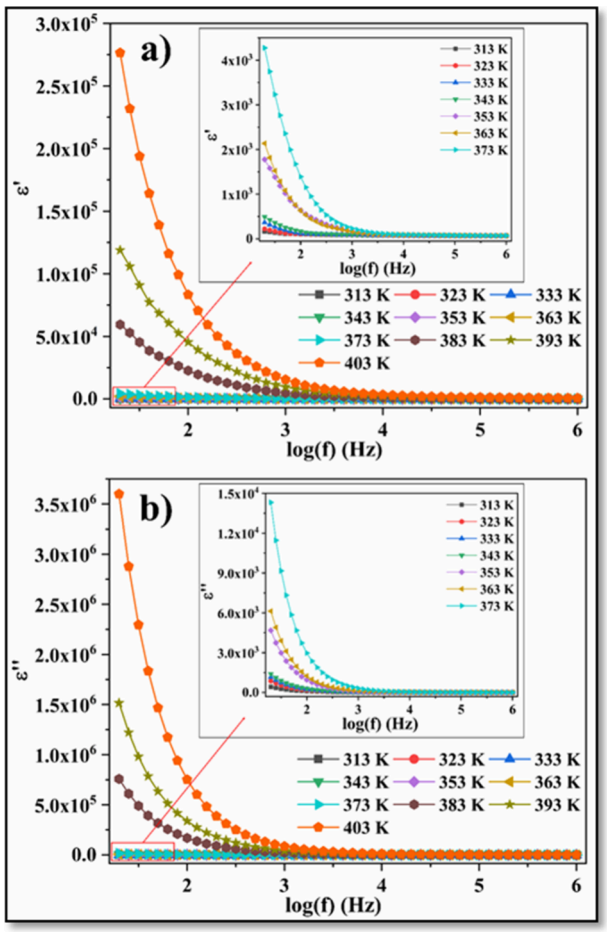

Figure 21. (a) Frequency dependence of the real part ε', (b) imaginary part ε'' of the permittivity at different temperatures for $(C_3H_8N_6)_2ZnCl_4{\cdot}2Cl$.

studied. High ε values may suggest charge accumulation at the sample−electrode contact.

Figure 22(a),(b) depict the temperature dependence of the real component (ε') and imaginary part (ε'') of permittivity at chosen frequencies. 20, 25, 32, 40, and 50 Hz.

Figure 22(a) shows that ε' decreases as frequency increases and increases with rising temperature. Prior to the phase transition, a slight depression is observed, followed by a relatively stable stage. This behavior is likely due to the restricted reorientational motion of the cationic part, which struggles to align with the applied electric field direction.

In Figure 22(b), ε'' increases notably with temperature above T_2 = 373 K. This increase can be attributed to factors such as the reorientation of $(C_3H_8N_6)$ groups and enhanced mobility of charge carriers, contributing to increased dissipation of energy.[96]

4.6.2. Complex Modulus Analysis. The concept of complex modulus provides essential insights into how materials transport charges and undergo relaxation processes, especially in relation to electrode polarization conductivity and relaxation phenomena.[94] The electric modulus (M^*) is defined as

$$M^* = M' + jM''$$

where $M' = -\omega C_0 Z''$, $M'' = \omega C_0 Z'$, and ω represents the angular frequency ($2\pi f$).

https://doi.org/10.1021/acsomega.4c06685
ACS Omega 2024, 9, 47597−47612

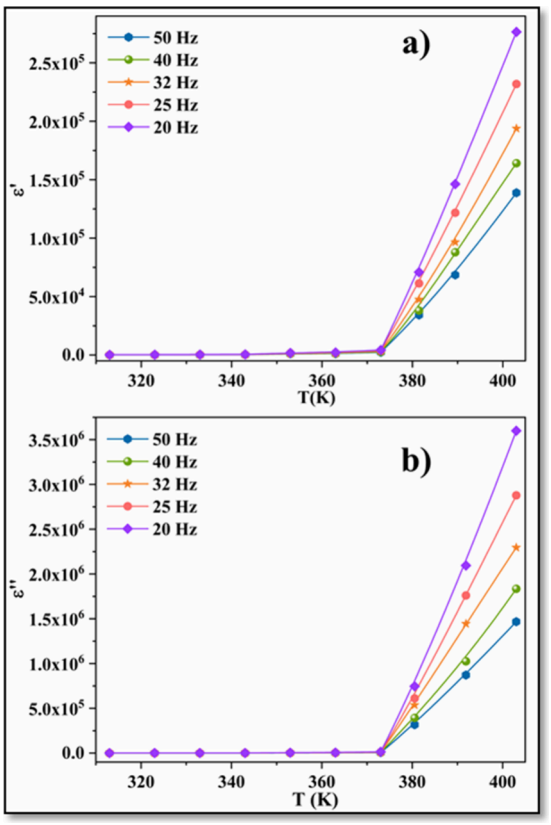

Figure 22. Temperature dependence of the (a) real and (b) imaginary parts of dielectric permittivity of $(C_3H_8N_6)_2ZnCl_4{\cdot}2Cl$, at different frequencies.

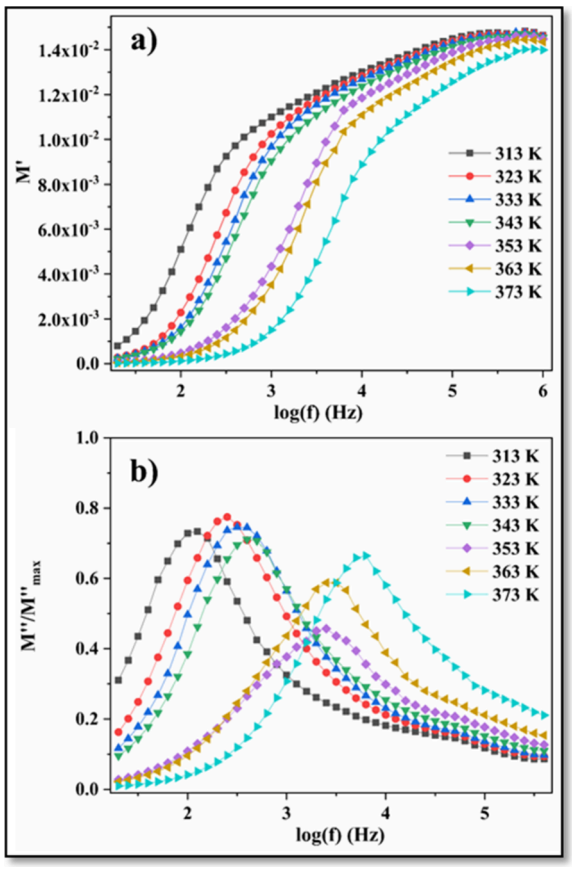

Figure 23. Variation of M' (a) and M''/M''_{max} (b) as a function of the log (f) at various temperatures in $(C_3H_8N_6)_2ZnCl_4{\cdot}2Cl$.

Figure 23(a),(b) depicts the real component (M') and the normalized imaginary component (M''/M''_{max}) of the electrical modulus as a function of frequency at various temperatures.

In Figure 23(a), M' exhibits frequency dependence across different temperatures. At higher frequencies, M' stabilizes to a constant value ($M'_\infty \approx \frac{1}{\varepsilon'_\infty}$), indicating minimal resistance to the move of charge carriers under an induced electric field. Thus, the conduction mechanism likely involves long-range mobility of charge carriers.[97]

Moreover, Figure 23(b) shows M''/M''_{max} spectra for a specific temperature, characterized by an asymmetric peak. As temperature rises, the peak maximum shifts to higher frequencies. The left side of the spectra corresponds to the long-range movement of charge carriers, predominantly H^+, over extended distances, while the right side reflects their confinement within potential wells. The migration from long-range to short-range mobility as the frequency decreases occurs near the relaxation frequency, defined by $\omega\tau = 1$. τ is defined as the most predicted ion relaxation time[98]

The temperature dependence of log (fp) is shown in Figure 24, where the frequency in relation to the M'_{max} peak associated with bulk relaxation is represented by $fp = 1/2\pi\tau f$.

The graph adheres to an Arrhenius-type law ($\sigma T = \sigma_0 \exp(-E_a/k_B T)$), indicating parallel behavior between log ($\sigma_{dc}T$) conductivity and log(fp) modulus peak maxima over the observed temperature range. Consequently, the activation energies obtained from impedance (E_a) and modulus (E_r) spectra are closely aligned, suggesting that H^+ ion transport in the material likely occurs via a hopping mechanism.[95]

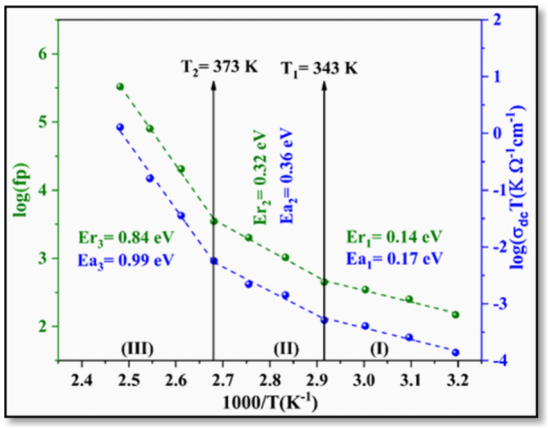

Figure 24. Temperature dependences of log($\sigma_{dc}T$) and log fp of $(C_3H_8N_6)_2ZnCl_4{\cdot}2Cl$.

CONCLUSION

In summary, we successfully synthesized single crystals of $(C_3H_8N_6)_2ZnCl_4{\cdot}2Cl$ by using the slow evaporation method. These crystals adopt a monoclinic crystal structure in the $P2_1/c$ space group, as confirmed by scanning electron microscopy (SEM), energy-dispersive X-ray analysis (EDX), and X-ray diffraction (XRD) for purity and crystallinity assessment. The crystal structure features alternating layers of $(C_3H_8N_6)^{2+}$ cations, $[ZnCl_4]^{2-}$ anionic tetrahedra, and isolated chloride anions, stabilized by N−H···Cl and N−H···N hydrogen bonds.

https://doi.org/10.1021/acsomega.4c06685
ACS Omega 2024, 9, 47597−47612

Our analysis included Hirshfeld surface studies, revealing predominant hydrogen bond interactions such as H···Cl/Cl···H and N···H/H···N within the crystal lattice. IR and Raman spectroscopy confirmed the existence of the two organic and inorganic components. Differential scanning calorimetry (DSC) identified two phase transitions: one at T_1 = 343 K and another of the order−disorder type at T_2 = 358 K, corroborated by subsequent dielectric and electrical property investigations.

Complex impedance analysis provided insights into the material's electrical behavior across varying temperatures and frequencies, revealing it as an excellent protonic conductor. Dielectric studies indicated a characteristic relaxation behavior typical of such materials.

■ ASSOCIATED CONTENT

Data Availability Statement

CDCC 2372132 contains the supplementary crystallographic data for the title compound.

Supporting Information

The Supporting Information is available free of charge at https://pubs.acs.org/doi/10.1021/acsomega.4c06685.

Atomic coordinates and equivalent isotropic displacement parameters (Å^2), anisotropic thermal agitation factors (Å^2) and selected bond distances (Å) and angles (deg) of the compound $(C_3H_8N_6)_2ZnCl_4{\cdot}2Cl$ (PDF)

■ AUTHOR INFORMATION

Corresponding Author

Mohamed Dammak − *Laboratory of Inorganic Chemistry (LCI) LR17ES07, Faculty of Sciences of Sfax, University of Sfax, 3000 Sfax, Tunisia;* orcid.org/0009-0004-7712-640X; Email: meddammak@yahoo.fr

Authors

Sahar Zaghden − *Laboratory of Inorganic Chemistry (LCI) LR17ES07, Faculty of Sciences of Sfax, University of Sfax, 3000 Sfax, Tunisia*

Hadhemi Ben Attia − *Laboratory of Inorganic Chemistry (LCI) LR17ES07, Faculty of Sciences of Sfax, University of Sfax, 3000 Sfax, Tunisia; Department of Physical and Analytical Chemistry, Oviedo University-CINN, 33006 Oviedo, Spain*

Mohammed S. M. Abdelbaky − *Department of Physical and Analytical Chemistry, Oviedo University-CINN, 33006 Oviedo, Spain; Department of Physical Chemistry, Faculty of Chemical Science, University of Salamanca, E-37008 Salamanca, Spain*

Abderrazek Oueslati − *Laboratory of Spectroscopy and Optical Characterizations of Materials, Faculty of Sciences of Sfax, University of Sfax, 3000 Sfax, Tunisia;* orcid.org/0000-0002-3221-3401

Santiago García-Granda − *Department of Physical and Analytical Chemistry, Oviedo University-CINN, 33006 Oviedo, Spain;* orcid.org/0000-0002-2373-0247

Lilia Ktari − *Laboratory of Inorganic Chemistry (LCI) LR17ES07, Faculty of Sciences of Sfax, University of Sfax, 3000 Sfax, Tunisia*

Complete contact information is available at: https://pubs.acs.org/10.1021/acsomega.4c06685

Author Contributions

All authors contributed to the discussions and revisions of the manuscript. S.Z.: Characterization, writing, original draft, methodology, data curation, conceptualization. H.B.A.: Conceptualization, characterization, writing, review validation. M.S.A.: Data curation, Investigation. A.O.: Original draft, data curation. S.G.G.: Data curation, Investigation. M.D.: Validation, supervision. K.L.: Validation, supervision.

Notes

The authors declare no competing financial interest.

■ ACKNOWLEDGMENTS

The Minister of Superior Education and Research of Tunisia and Spanish Ministerio de Ciencia e Innovacion (PID2020-113558RB-C41) and Gobierno del Principado de Asturias (GRUPIN-2021/50997) are acknowledged.

■ REFERENCES

(1) Mala, N.; Dar, M.; Rather, M. U.; Sivakumar, S.; Husain, S.; Batoo, K. Enhanced Electrochemical Properties of Zinc and Manganese Co-Doped NiO Nanostructures for Its High-Performance Supercapacitor Applications. *Inorg. Chem. Commun.* **2022**, *142*, 109661.

(2) Sivakumar, S.; Mala, N.; Batoo, K.; Ijaz, M. Conserved Crystal Phase and Morphology: Electrochemical Supremacy of Copper (Cu) and Iron (Fe) Dual-Doped Nickel Oxide and Its Supercapacitor Applications. *Inorg. Chem. Commun.* **2021**, *134*, 108959.

(3) Mala, N.; Sivakumar, S.; Batoo, K.; Hadi, M. Design and Fabrication of Iron-Doped Nickel Oxide-Based Flexible Electrode for High-Performance Energy Storage Applications. *Inorg. Chem. Commun.* **2021**, *131*, 108797.

(4) Benali-Cherif, R.; Takouachet, R.; Falek, W.; Benali-Cherif, N.; Jelsch, C.; Merazig, H.; Hafied, M.; Bendeif, E.-E.; Mokhnachi, N. B.; Taibi, K. Synthesis, Structural Elucidation, Spectroscopic, Hirshfeld Surface Analysis and Theoretical Simulation of a New Adeninium Orthoperiodate (1-) Bis(Hydrate) Organic-Inorganic Hybrid Crystals. *J. Mol. Struct.* **2021**, *1224*, 129034.

(5) Kessentini, A.; Belhouchet, M.; Suñol, J. J.; Abid, Y.; Mhiri, T. Synthesis, Crystal Structure, Vibrational Spectra, Optical Properties and Theoretical Investigation of Bis (2-Aminobenzimidazolium) Tetraiodocadmate. *J. Mol. Struct.* **2013**, *1039*, 207−213.

(6) Chaabane, I.; Hlel, F.; Guidara, K. Electrical Study by Impedance Spectroscopy of the New Compound $[C_{12}H_{17}N_2]_2CdCl_4$. *J. Alloys Compd.* **2008**, *461*, 495−500.

(7) Moulahi, A.; Guesmi, O.; Abdelbaky, M.; García-Granda, S.; Dammak, M. Structural Characterization, Thermal Analysis, Electric and Dielectric Properties of a Novel Organic-Inorganic Hybrid Compound Based on Iron Fluoride. *J. Alloys Compd.* **2022**, *898*, 162956.

(8) Arjunan, V.; Marchewka, M.; Kalaivani, M. Synthesis, Vibrational and Quantum Chemical Investigations of Hydrogen Bonded Complex Betaine Dihydrogen Selenite. *Spectrochimica acta. Part A, Molecular and biomolecular spectroscopy* **2012**, *96*, 744−758.

(9) Grombein, C. M.; Hu, Q.; Heim, R.; Rau, S.; Zimmer, C.; Hartmann, R. W. 1-Phenylsulfinyl-3-(Pyridin-3-Yl)Naphthalen-2-Ols: A New Class of Potent and Selective Aldosterone Synthase Inhibitors. *Eur. J. Med. Chem.* **2015**, *89*, 597−605.

(10) Barraja, P.; Diana, P.; Spanò, V.; Montalbano, A.; Carbone, A.; Parrino, B.; Cirrincione, G. An Efficient Synthesis of Pyrrolo[3′,2′:4,5]-Thiopyrano[3,2-b]Pyridin-2-One: A New Ring System of Pharmaceutical Interest. *Tetrahedron* **2012**, *68*, 5087−5094.

(11) Jomaa, I.; Issaoui, N.; Roisnel, T.; Marouani, H. Assembly of Two New Hybrid Chloride Materials with Potential NLO Properties: Structure Elucidation, Empirical and Computational Studies. *Journal of the Iranian Chemical Society* **2022**, *19* (6), 2527−2542.

(12) Bentahar, F.; Abdelbaky, M. S. M.; Isabel Menéndez, M.; Huidobro, P.; García-Granda, S.; Dammak, M. A Novel Antibacterial

Benzimidazolium Hexachlorotellurate Hybrid Compound: Experimental-Theoretical Characterization. *Polyhedron* **2022**, *228*, 116034.
(13) Zhu, X.-F.; Shi, D.-Q. Convenient Synthesis and Biological Activities of Pyridine Derivatives of 3,4-Dihydropyrimidin-2(1H)-Ones. *Journal of Heterocyclic Chemistry* **2011**, *48* (3), 572−576.
(14) Vijayakanth, T.; Liptrot, D. J.; Gazit, E.; Boomishankar, R.; Bowen, C. R. Recent Advances in Organic and Organic-Inorganic Hybrid Materials for Piezoelectric Mechanical Energy Harvesting. *Adv. Funct. Mater.* **2022**, *32* (17), 2109492.
(15) Zhao, X.; Du, Y.; Li, W.; Zhao, Z.; Lei, M. Organic/Inorganic Hybrids for Intelligent Sensing and Wearable Clean Energy Applications. *Adv. Compos. Hybrid. Mater.* **2023**, *6* (5), 176.
(16) Liu, J.; Chen, X.; Yang, H.; Shan, K. Hybrid Renewable Energy Applications in Zero-Energy Buildings and Communities Integrating Battery and Hydrogen Vehicle Storage. *Appl. Energy* **2021**, *290*, 116733.
(17) Mohammadi, M.; Khodamorady, M.; Tahmasbi, B.; Bahrami, K.; Ghorbani-Choghamarani, A. Boehmite Nanoparticles as Versatile Support for Organic-Inorganic Hybrid Materials: Synthesis, Functionalization, and Applications in Eco-Friendly Catalysis. *J. Ind. Eng. Chem.* **2021**, *97*, 1−78.
(18) Mao, W.; Wang, J.; Liao, H.; Zhou, B.; Zheng, G.; Mo, S.; Long, F.; Zou, Z. Crystal Structure and Electrical Conduction of the Organic-Inorganic Compound $(C_6H_9N_2)_2ZnI_4$. *Polyhedron* **2019**, *164*, 48.
(19) Yuan, W.; Zeng, Y.; Tan, Y.-Y.; Zhou, J.-H.; Xu, W.-J.; Zhang, W.-X.; Chen, X.-M. A New Ferroelastic Hybrid Material with a Large Spontaneous Strain: $(Me_3NOH)_2[ZnCl_4]$. *Chem. Commun.* **2019**, *55* (61), 8983−8986.
(20) Fu, D.; Xin, J.; He, Y.; Wu, S.; Zhang, X.; Zhang, X.-M.; Luo, J. Chirality-Dependent Second-Order Nonlinear Optical Effect in 1D Organic-Inorganic Hybrid Perovskite Bulk Single Crystal. *Angew. Chem., Int. Ed.* **2021**, *60* (36), 20021−20026.
(21) Xu, K.; He, L.; Wang, Y.-Z.; Meng, X.; Shi, P.-P.; Ye, Q. $(C_7H_{18}N_2)PbI_4$: A 2D Hybrid Perovskite Solid-State Phase Transition Material with Semiconducting Properties. *Inorg. Chem.* **2021**, *60* (14), 10642−10647.
(22) Li, J.; Zhu, Y.; Huang, P.-Z.; Fu, D.-W.; Jia, Q.-Q.; Lu, H.-F. Ferroelasticity in Organic-Inorganic Hybrid Perovskites. *Chem.—Eur. J.* **2022**, *28* (59), No. e202201005.
(23) Said, M.; Boughzala, H. Synthesis, Crystal Structure, Hirshfeld Surface Analysis, Spectroscopic, Optical and Thermal Behavior of New Organic-Inorganic Hybrid Material $(C_7H_{11}N_2)_2[CrCl_2(H_2O)_4]Cl_3 \cdot 2H_2O$. *J. Mol. Struct.* **2019**, *1189*, 122−130.
(24) Messoudi, N.; Messoudi, N.; Elleuch, S.; Jarraya, K. Structure study, Hirshfeld surface analysis, thermal, vibrational and DFT investigation of 2, 4, 6-triamino-1, 3, 5-triazin-1-ium selenite. *J. Struct. Chem.* **2021**, *62* (8), 1293−1308.
(25) Elfaleh, N.; Karoui, S.; Kamoun, S. Ionic Conductivities and Dielectric Analysis of $(C_6H_{20}N_3)BiI_6.H_2O$ Compound. *Indian Journal of Physics* **2022**, *96*, 2337−2344.
(26) Kahouli, K.; Mesbeh, R.; Abdelbaky, M. S. M.; Garcia-Granda, S.; Koumina, A.; Chaabouni, S. Crystal Structure, Hirshfeld Surface Analysis, Vibrational and Optical Properties of Organic-Inorganic Hybrid Compound $(C_{13}H_{16}N_2)_5(BiCl_6)3\bullet Cl$. *J. Mol. Struct.* **2021**, *1231*, 129826.
(27) Salah, T.; Ahmed, A. B.; Krayem, N.; Guesmi, A.; Hamadi, N. B.; Khezami, L.; Naïli, H.; Hamdi, B. Two Different Coordination Polyhedra in the Crystal Structure of a Novel Zn (II) Hybrid Complex: DFT Investigation, Biological Activities and Emission Properties. *J. Mol. Struct.* **2024**, *1296*, 136863.
(28) Morales, A.; Durán, A. Sol-Gel Protection of Front Surface Silver and Aluminum Mirrors. *J. Sol-Gel Sci. Technol.* **1997**, *8* (1), 451−457.
(29) Walcarius, A. Electrochemical Applications of Silica-Based Organic-Inorganic Hybrid Materials. *Chem. Mater.* **2001**, *13*, 3351−3372.
(30) Wight, A. P.; Davis, M. E. Design and Preparation of Organic-Inorganic Hybrid Catalysts. *Chem. Rev.* **2002**, *102* (10), 3589−3613.
(31) Yang, G.; Tao, H.; Qin, P.; Ke, W.; Fang, G. Recent Progress in Electron Transport Layers for Efficient Perovskite Solar Cells. *J. Mater. Chem. A* **2016**, *4* (11), 3970−3990.
(32) Azadmanjiri, J.; Berndt, C. C.; Wang, J.; Kapoor, A.; Srivastava, V. K.; Wen, C. A Review on Hybrid Nanolaminate Materials Synthesized by Deposition Techniques for Energy Storage Applications. *J. Mater. Chem. A* **2014**, *2* (11), 3695−3708.
(33) Sanchez, C.; Shea, K. J.; Kitagawa, S. Recent Progress in Hybrid Materials Science. *Chem. Soc. Rev.* **2011**, *40* (2), 471−472.
(34) Ayari, C.; Alotaibi, A. A.; Baashen, M. A.; Perveen, F.; Almarri, A. H.; Alotaibi, K. M.; Abdelbaky, M. S. M.; Garcia-Granda, S.; Othmani, A.; Nasr, C. B.; Mrad, M. H. A New Zn (II) Metal Hybrid Material of 5-Nitrobenzimidazolium Organic Cation $(C_7H_6N_3O_2)_2[ZnCl_4]$: Elaboration, Structure, Hirshfeld Surface, Spectroscopic, Molecular Docking Analysis, Electric and Dielectric Properties. *Materials (Basel)* **2022**, *15* (22), 7973.
(35) Chihaoui, N.; Hamdi, B.; Zouari, R. Structural Elucidation, Theoretical Investigation Using DFT Calculations, Thermal and Dielectric Analyses of New Zinc (II) Based Inorganic-Organic Hybrid. *Chin. Chem. Lett.* **2017**, *28*, 642−650.
(36) Mahfoudh, N.; Karoui, K.; BenRhaiem, A. Optical Studies and Dielectric Response of $[DMA]_2MCl_4$ (M = Zn and Co) and $[DMA]_2ZnBr_4$. *RSC Adv.* **2021**, *11* (40), 24526−24535.
(37) Burlov, A. S.; Vlasenko, V. G.; Koshchienko, Y. V.; Milutka, M. S.; Mal'tsev, E. I.; Dmitriev, A. V.; Lypenko, D. A.; Nekrasova, N. V.; Kolodina, A. A.; Makarova, N. I.; Metelitsa, A. V.; Lazarenko, V. A.; Zubavichus, Y. V.; Khrustalev, V. N.; Garnovskii, D. A. Synthesis, Structure, and Photoluminescent and Electroluminescent Properties of Zinc (II) Complexes with Bidentate Azomethine Ligands. *Appl. Organomet. Chem.* **2021**, *35* (2), No. e6107.
(38) Gusev, A.; Braga, E.; Tyutyunik, A.; Gurchenko, V.; Berezovskaya, M.; Kryukova, M.; Kiskin, M.; Linert, W. Synthesis, Photoluminescence and Electrical Study of Pyrazolone-Based Azomethine Ligand Zn (II) Complexes. *Materials (Basel)* **2020**, *13* (24), 5698.
(39) Chen, L.; Liao, W.-Q.; Ai, Y.; Li, J.; Deng, S.; Hou, Y.; Tang, Y.-Y. Precise Molecular Design Toward Organic-Inorganic Zinc Chloride ABX3 Ferroelectrics. *J. Am. Chem. Soc.* **2020**, *142* (13), 6236−6243.
(40) Sanchez, C.; Julián, B.; Belleville, P.; Popall, M. Applications of Hybrid Organic-Inorganic Nanocomposites. *J. Mater. Chem.* **2005**, *15* (35−36), 3559−3592.
(41) Meng, X.; Liu, Z.-B.; Xu, K.; He, L.; Wang, Y.-Z.; Shi, P.-P.; Ye, Q. Metal Regulated Organic-Inorganic Hybrid Ferroelastic Materials: $[(CH_3)_3CN(CH_3)_2CH_2F]_2[MBr_4]$ (M = Cd and Zn). *Inorg. Chem. Front.* **2022**, *9* (8), 1603−1608.
(42) Gomila, R. M.; Bauzá, A.; Mooibroek, T. J.; Frontera, A. Spodium Bonding in Five Coordinated Zn(II): A New Player in Crystal Engineering? *CrystEngComm* **2021**, *23* (17), 3084−3093.
(43) Sakiyama, H.; Abiko, T.; Ito, M.; Mitsuhashi, R.; Mikuriya, M.; Waki, K. Conformational Analysis of an Octahedral Zinc(II) Complex with Six Dimethylsulfoxide. *Polyhedron* **2016**, *119*, 512−516.
(44) Prabhaharan, M.; Prabakaran, A. R.; Gunasekaran, S.; Srinivasan, S. Molecular Structure and Vibrational Spectroscopic Investigation of Melamine Using DFT Theory Calculations. *Spectrochimica Acta Part A: Molecular and Biomolecular Spectroscopy* **2014**, *123*, 392−401.
(45) Snyder, F. *Three Worlds of Melamine*; Brill, 2016; pp 9−107.
(46) Zięba-Palus, J. Application of Micro-Fourier Transform Infrared Spectroscopy to the Examination of Paint Samples. *J. Mol. Struct.* **1999**, *511−512*, 327−335.
(47) Mesbeh, R.; Hamdi, B.; Zouari, R. Elaboration, Structural, Vibrational, DSC Investigations and Hirshfeld Surface Analysis of New Organic-Inorganic Hybrid Compound: $[H_2mela]Cu_2Br_6$. *J. Clust. Sci.* **2016**, *27* (5), 1751−1762.
(48) Weng, D.-F.; Wang, B.-W.; Wang, Z.-M.; Gao, S. $(H_2mela)_2[FeCl_5]Cl$ (Mela = melamine): A Cl-Bridged Single-Chain Magnet Based on Weak Ferromagnetism. *Coord. Chem. Rev.* **2013**, *257*, 2484−2490.
(49) Mesbeh, R.; Hamdi, B.; Zouari, R. Elaboration, Structural, Spectroscopy, DSC Investigations and Hirshfeld Surface Analysis of a One-Dimensional Self-Assembled Organic-Inorganic Hybrid Compound. *J. Mol. Struct.* **2017**, *1128*, 205−214.
(50) Araar, H.; Benounis, M.; Direm, A.; Touati, A.; Atailia, S.; Barhoumi, H.; Jaffrezic-Renault, N. A New Thin Film Modified Glassy

https://doi.org/10.1021/acsomega.4c06685
ACS Omega 2024, 9, 47597−47612

Carbon Electrode Based on Melaminium Chloride Pentachlorocuprate(II) for Selective Determination of Nitrate in Water. *Monatsh. Chem.* **2019**, *150* (10), 1737−1744.
(51) Hamdi, B.; Zouari, R.; Ben Salah, A. Synthesis, Crystal Structure, Hirshfeld Surface Analyses and Physical Properties of a New Hybrid Compound: $[C_3N_6H_8]_2PbCl_5.Cl$. *Superlattices Microstruct.* **2018**, *123*, 97−110.
(52) Lu, J.; Lian, Y.-K.; Xiong, L.; Wu, Q.-R.; Zhao, M.; Shi, K.-X.; Chen, L.; Wu, L.-M. How To Maximize Birefringence and Nonlinearity of π-Conjugated Cyanurates. *J. Am. Chem. Soc.* **2019**, *141* (40), 16151−16159.
(53) Ben Attia, H.; Bentahar, F.; Abdelbaky, M. S. M.; Elferjani, A.; García-Granda, S.; Dammak, M. Phase Transitions, Thermal, Vibrational (FT-IR and Raman) and Optical Characterizations, Dielectric Relaxation and Electrical Conductivity of a Cobalt (II) Based Hybrid Material. *J. Alloys Compd.* **2023**, *969*, 172317.
(54) Maraii, D.; Dammak, M. Synthesis, Structure, Optical and Thermal Analysis of the New Compound of the New Compound Organo-Metallic $(C_5H_6N)_2TeCl_6$. *J. Mol. Struct.* **2022**, *1247*, 131282.
(55) Bourhis, L. J.; Dolomanov, O. V.; Gildea, R. J.; Howard, J. a. K.; Puschmann, H. OLEX2: A Complete Structure Solution, Refinement and Analysis Program. *J. Appl. Crystallogr.* **2009**, *42* (2), 339−341.
(56) Sheldrick, G. M. Crystal Structure Refinement with SHELXL. *Acta. Cryst. C* **2015**, *71* (1), 3−8.
(57) Sheldrick, G. M. SHELXT - Integrated Space-Group and Crystal-Structure Determination. *Acta. Cryst. A* **2015**, *71* (1), 3−8.
(58) Brandenburg, K.; Putz, H. *DIAMOND* (Release 3.2 c); Crystal Impact GbR: Bonn, Germany, 2006.
(59) Farrugia, L. J. WinGX and ORTEP for Windows: An Update. *J. Appl. Crystallogr.* **2012**, *45* (4), 849−854.
(60) Roisnel, T.; Rodríguez-Carvajal, J. WinPLOTR, a Graphic Tool for Powder Diffraction. *J. Mater. Sci. Forum* **2001**, *378-381*, 118.
(61) Salah, T.; Mhadhbi, N.; Ben Ahmed, A.; Hamdi, B.; Krayem, N.; Loukil, M.; Guesmi, A.; Khezami, L.; Houas, A.; Ben Hamadi, N.; Naïli, H.; Costantino, F. Physico-Chemical Characterization, DFT Modeling and Biological Activities of a New Zn (II) Complex Containing Melamine as a Template. *Crystals* **2023**, *13*, 746.
(62) Chen, S.; Zhu, Y.; Wei, X.; Zheng, G.; Zhao, Q.; Mo, S.; Wang, J.; Yao, D.; Tian, N.; Long, F. Crystal Structure, Hirshfeld Surface Analysis, Optical Properties and Stability of Organic-Inorganic Compound $(C_6H_5CH_2NH_3)_2(CH_3CH_3NH_2)_3Bi_2Br_{11}$. *Journal of Solid-State Chemistry France* **2024**, *330*, 124482.
(63) Wolff, S. K.; Grimwood, D. J.; McKinnon, J. J.; Turner, M. J.; Jayatilaka, D.; Spackman, M. A. *Crystal Explorer* 3.0; University of Western Australia, 2012.
(64) Hannachi, N.; Elwej, R.; Roisnel, T.; Hlel, F. Effect of Changing Anion on the Crystalline Structure, Crystal Structure, Hirschfield Surface, IR and NMR Spectroscopy of Organic Salts and Hybrid Compounds: $C_6H_4(NH_3)_2Cl_2$ (I), β-$[C_6H_{10}N_2]_2ZnCl_4$ (II), Respectively. *Open J. Inorg. Chem.* **2023**, *13*, 1−24.
(65) Jellali, A.; Karâa, N.; Ghalla, H.; Hamdi, B. Physical and Chemical Characterisations, Optical Properties and Dielectric Studies of a New Organic-Inorganic Material: Bis(4-Amino-2-Chloropyridinium) Tetrachloromercurate (II) Monohydrate. *Chemistry Africa* **2024**, *7* (3), 1649−1665.
(66) Seth, S. K. Structural Elucidation and Contribution of Intermolecular Interactions in O-Hydroxy Acyl Aromatics: Insights from X-Ray and Hirshfeld Surface Analysis. *J. Mol. Struct.* **2014**, *1064*, 70−75.
(67) Baur, W. H.; Tillmanns, E. Salt Hydrates. X. The Crystal Structure Determinations of Heptasodium Fluoride Bisphosphate 19-Hydrate and Heptasodium Fluoride Bisarsenate 19-Hydrate and the Computer Simulation of the Isomorphous Vanadate Salt. *Acta. Cryst. B* **1974**, *30* (9), 2218−2224.
(68) Hannachi, N.; Elwej, R.; Roisnel, T.; Hlel, F. Effect of Changing Anion on the Crystalline Structure, Crystal Structure, Hirschfield Surface, IR and NMR Spectroscopy of Organic Salts and Hybrid Compounds: $C_6H_4(NH_3)_2Cl_2$ (I), β-$[C_6H_{10}N_2]_2ZnCl_4$ (II), Respectively. *Open Journal of Inorganic Chemistry* **2023**, *13* (1), 1−24.
(69) El Glaoui, M.; El Glaoui, M.; Jelsch, C.; Aubert, E.; Lefebvre, F.; Ben Nasr, C. A Hirshfeld Surface Analysis, Crystal Structure and Spectroscopic Properties of New Zn (II) Complex with N-Amino-ethylpiperazine Ligand. *J. Mol. Struct.* **2017**, *1134*, 538−545.
(70) Elleuch, N.; Fredj, D.; Chniba-Boudjada, N.; Boujelbene, M. Synthesis of a New Chloro Antimony Complex with Pyridinium Derivative: Crystal Structure, Hirshfeld Surface Analysis, Vibrational, and Optical Properties. *J. Inorg. Organomet. Polym.* **2020**, *30* (3), 889−898.
(71) Janiak, C. A Critical Account on π-π Stacking in Metal Complexes with Aromatic Nitrogen-Containing Ligands. *J. Chem. Soc., Dalton Trans.* **2000**, No. 21, 3885−3896.
(72) Bernstein, J.; Davis, R. E.; Shimoni, L.; Chang, N.-L. Patterns in Hydrogen Bonding: Functionality and Graph Set Analysis in Crystals. *Angewandte Chemie International Edition in English* **1995**, *34* (15), 1555−1573.
(73) Brown, I. D. On the Geometry of O-H···O Hydrogen Bonds. *Acta Cryst. A* **1976**, *32* (1), 24−31.
(74) Ben Hadj Sadok, I.; Hajlaoui, F.; Karoui, K.; Audebrand, N.; Roisnel, T.; Zouari, N. Crystal Structure, Optical and Electrical Properties of Metal-Halide Compound $[C_7H_{16}N_2][ZnCl_4]$. *J. Phys. Chem. Solids* **2019**, *129*, 71−80.
(75) Mesbeh, R.; Hamdi, B.; Zouari, R. $(H_2pdcCuBr_2)_2$•2(MH^+) •2Br^- (M = Melamine, H2pdc = Pyridine-2,6-Dicarboxylic Acid): Crystal Structure, Hirshfeld Surface Analysis, Vibrational and Thermal Studies. *J. Inorg. Organomet. Polym.* **2016**, *26* (4), 744−755.
(76) Weng, D.-F.; Wang, B.-W.; Wang, Z.-M.; Gao, S. Polymorphism of $(H_2mela)_2[CuCl_5]Cl$ (Mela = Melamine): Structures, Transformation and Magnetic Properties. *CrystEngComm* **2011**, *13*, 4683−4688.
(77) Khadri, A.; Bouchene, R.; Bouacida, S.; Sid, A.; Alswaidan, I. A.; Ramasami, P. Synthesis, Structural, Thermal, Hirshfeld Surface and DFT Studies on a New Hybrid Compound: Bis[4-(Dimethylamino)-Pyridinium] Tetrachloridomanganate(II). *J. Coord. Chem.* **2020**, *73* (4), 609−621.
(78) Sakka, A.; Jellali, A.; Hamdi, B.; Abdelbaky, M. S. M.; Naïli, H.; García-Granda, S.; Zouari, R. Structure, Spectroscopic Measurement, Thermal Studies and Optical Properties of a New Non-Centrosymmetric Hybrid Compound. *J. Mol. Struct.* **2019**, *1198*, 126867.
(79) Chihaoui, N.; Hamdi, B. A New Mononuclear Complex: Structure, Vibrational (FT-IR and Raman), Hirshfeld Surfaces Analysis, Electrical Properties and Equivalent Circuit. *J. Phys. Chem. Biophys.* **2016**, *6*, 2161.
(80) Ben Mohamed, C.; Karoui, K.; Bulou, A.; Ben Rhaiem, A. Raman Studies of Phase Transitions in Ferroelectric $[C_2H_5NH_3]_2ZnCl_4$. *Physica E: Low-dimensional Systems and Nanostructures* **2017**, *87*, 141−149.
(81) Mahfoudh, N.; Karoui, K.; Khirouni, K.; Ben Rhaiem, A. Optical, Electrical Properties and Conduction Mechanism of $[(CH_3)_2NH_2]_2ZnCl_4$ Compound. *Physica B Condensed Matter* **2019**, *554*, 126−136.
(82) Ben Bechir, M.; Karoui, K.; Bulou, A.; Tabellout, M.; Guidara, K.; Ben Rhaiem, A. $[N(CH_3)_3H]_2ZnCl_4$: Ferroelectric Properties and Characterization of Phase Transitions by Raman Spectroscopy. *J. Appl. Phys.* **2014**, *116* (21), 214104.
(83) Ben Gzaiel, M.; Oueslati, A.; Lhoste, J.; Gargouri, M.; Bulou, A. Synthesis, Crystal Structure and High Temperature Phase Transition in the New Organic-Inorganic Hybrid $[N(C_4H_9)_4]_3Zn_2Cl_7H_2O$ Crystals. *J. Mol. Struct.* **2015**, *1089*, 153−160.
(84) Kammoun, I.; Belhouchet, M.; Ben Ahmed, A.; Lhoste, J.; Gargouri, M. Investigation of Structural, Optical and Electrical Conductivity of a New Organic Inorganic Bromide: $[C_{12}H_{17}N]_2ZnBr_4$. *RSC Adv.* **2023**, *13* (12), 8034−8042.
(85) Alotaibi, A.; Hermi, S.; Perveen, F.; Othmani, A.; Hassan, H.; Kaminsky, W.; Nasr, C.; Mrad, M. H. New Hybrid Material's Structure, Electric-Dielectric Properties, Spectroscopic Analysis, DN A Interactions, and Antibacterial Application of Bis-(5-Nitrobenzimidzolium) Tetrachlorozincate Monohydrate. *Journal of Cluster Science* **2023**, *34*, 2711.

https://doi.org/10.1021/acsomega.4c06685
ACS Omega 2024, 9, 47597−47612

(86) Chihi, I.; Baazaoui, M.; Hamdaoui, N.; Greneche, J.-M.; Oumezzine, M.; Farah, K. Sol-Gel Synthesis and Characterization of Magnesium Ferrites by XRD, TEMEPR, Mossbauer, and Impedance Spectroscopy. *Journal of Materials Science: Materials in Electronics* **2021**, *32*, 16634.
(87) Kahouli, K.; kahouli, A.; Khirouni, K.; Chaabouni, S. Crystal Structure, Thermal Studies, Vibrational Properties, Atomic Hirshfeld Surface, and Electrical and Dielectric Studies of $[C_9H_{14}N]_3BiCl_6$ Single Crystal. *J. Mol. Struct.* **2020**, *1199*, 126944.
(88) Elgahami, H.; Lhoste, J.; Auguste, S.; Corbel, G.; Oueslati, A. Structural Phase Transition, Optical and Electrical Properties of the Hybrid Material $[(C_2H_5)_4N]_2ZnI_4$. *Journal of Solid State Chemistry France* **2022**, *314*, 123357.
(89) Ben Mohamed, C.; Karoui, K.; Tabellout, M.; Ben Rhaiem, A. Electrical, Dielectric and Optical Properties of $[C_2H_5NH_3]_2ZnCl_4$ Compound. *J. Alloys Compd.* **2016**, *688*, 407−415.
(90) Abid, D.; Dhouib, I.; Guionneau, P.; Pechev, S.; Chaabane, I.; Daro, N.; Elaoud, Z. Proton Conduction Study of a New Selenate-Based Hybrid Compound. *J. Alloys Compd.* **2020**, *824*, 153826.
(91) Wang, J.; Sun, J.; Zhou, J.; Jin, K.; Fang, Q. Fluorinated and Thermo-Cross-Linked Polyhedral Oligomeric Silsesquioxanes: New Organic-Inorganic Hybrid Materials for High-Performance Dielectric Application. *ACS Appl. Mater. Interfaces* **2017**, *9* (14), 12782−12790.
(92) Ayouchi, R.; Leinen, D.; Martin, F.; Gabas, M.; Dalchiele, E.; Ramos-Barrado, J. R. Preparation and Characterization of Transparent ZnO Thin Films Obtained by Spray Pyrolysis. *Thin Solid Films* **2003**, *426* (1−2), 68−77.
(93) Papathanassiou, A. N. Novel Feature of the Universal Power Law Dispersion of the Ac Conductivity in Disordered Matter. *J. Non-Cryst. Solids* **2006**, *352*, 5444−5445.
(94) Abid, D.; Mjejri, I.; Oueslati, A.; Guionneau, P.; Pechev, S.; Daro, N.; Elaoud, Z. A Nickel-Based Semiconductor Hybrid Material with Significant Dielectric Constant for Electronic Capacitors. *ACS Omega* **2024**, *9* (11), 12743−12752.
(95) Salah, N.; Hamdi, B.; Bouzidia, N.; Salah, A. B. Crystal Structures, Hirshfeld Surface Analysis, Thermal Behavior and Dielectric Properties of a New Organic-Inorganic Hybrid $[C_6H_{10}(NH_3)_2]Cu_2Cl_8$. *J. Mol. Struct.* **2017**, *1149*, 414−425.
(96) Chihaoui, N.; Hamdi, B.; Zouari, R. Structural Study, Spectroscopic Analysis and Dielectric Proprieties of New Hybrid Organic-Inorganic Compound. *J. Mol. Struct.* **2017**, *1147*, 48−55.
(97) Trigui, W.; Oueslati, A.; Chaabane, I.; Corbel, G.; Hlel, F. Electrical Properties, Equivalent Circuit and Dielectric Relaxation Studies of $[(C_3H_7)_4N]_3Bi_3Cl_{12}$ Compound. *Applied physics. A, Materials science & processing* **2015**, *119* (2), 673−680.
(98) Bouketaya, S.; Elferjani, A.; Abdelbaky, M. S. M.; Dammak, M.; Garcia-Granda, S. Crystal Structure, Phase Transitions, Dielectric and Vibrational Studies and Photoluminescence Properties of a New Iron Fluoride Based on Bipyridine. *Journal of Solid-State Chemistry France* **2019**, *277*, 395−405.

https://doi.org/10.1021/acsomega.4c06685
ACS Omega 2024, 9, 47597−47612